

# HYDRODYNAMICS OF CORE-COLLAPSE SUPERNOVAE AT THE TRANSITION TO EXPLOSION. I. SPHERICAL SYMMETRY

RODRIGO FERNÁNDEZ<sup>1</sup>

Institute for Advanced Study, Einstein Drive, Princeton, NJ 08540, USA.

*Draft version February 25, 2024*

## ABSTRACT

We study the transition to runaway expansion of an initially stalled core-collapse supernova shock. The neutrino luminosity, mass accretion rate, and neutrinospheric radius are all treated as free parameters. In spherical symmetry, this transition is mediated by a global non-adiabatic instability that develops on the advection time and reaches non-linear amplitude. Here we perform high-resolution, time-dependent hydrodynamic simulations of stalled supernova shocks with realistic microphysics to analyze this transition. We find that radial instability is a sufficient condition for runaway expansion if the neutrinospheric parameters do not vary with time and if heating by the accretion luminosity is neglected. For a given unstable mode, transition to runaway occurs when fluid in the gain region reaches positive specific energy. We find approximate instability criteria that accurately describe the behavior of the system over a wide region of parameter space. The threshold neutrino luminosities are in general different than the limiting value for a steady-state solution. We hypothesize that multidimensional explosions arise from the excitation of unstable large-scale modes of the turbulent background flow, at threshold luminosities that are lower than in the laminar case.

*Subject headings:* supernovae: general — hydrodynamics — shock waves — instabilities

## 1. INTRODUCTION

Following collapse of the core in a massive star, a hydrodynamic shock is launched when the central region reaches nuclear density. Significant energy losses due to neutrino emission and dissociation of infalling nuclei drain this shock of thermal energy and cause it to stall (e.g., Bethe 1990). For slowly-rotating progenitors, the re-absorption of a small fraction of neutrinos carrying away the gravitational binding energy of the protoneutron star is thought to re-energize this shock and trigger an explosion (Bethe & Wilson 1985). However, ab-initio radiation-hydrodynamic simulations in spherical symmetry fail to produce this outcome for stars that form iron cores (Liebendörfer et al. 2001; Rampp & Janka 2002; Thompson et al. 2003; Sumiyoshi et al. 2005). Success is only obtained for progenitors at the lowest end of the mass range leading to core-collapse ( $\sim 8 - 10M_{\odot}$ , Kitaura et al. 2006; Burrows et al. 2007a).

Increasing the dimensionality of simulations improves conditions for explosion by enabling non-spherical hydrodynamic instabilities. In axisymmetry (2D), large scale shock oscillations combined with neutrino-driven convection lead to late-time – albeit somewhat marginal – explosions in representative stellar progenitors (Marek & Janka 2009 and references therein). A recent three-dimensional (3D) hydrodynamic study found that the extra spatial dimension could make conditions even more favorable, reducing the neutrino luminosity needed to start an explosion by  $\sim 20\%$  relative to axisymmetry (Nordhaus et al. 2010). The way in which hydrodynamic processes combine to cause this decrease is not well understood at present, however. In particular, a change in the methods and approximations employed can erase this dimensionality effect, suggesting that it may manifest only in some region of physical and/or numerical parameter space (Hanke et al. 2011). Given the marginality of 2D models, it is important to identify the conditions under which this addi-

tional reduction in neutrino luminosity occurs.

The purpose of this paper and its companion is to systematically examine the hydrodynamic processes responsible for the transition to explosion in a stalled core-collapse supernova shock. As a first step, we study here the spherically symmetric case. Taking advantage of the simplicity of the flow geometry and borrowing tools from stellar pulsation theory, we develop a framework for identifying the relevant processes involved. The spherically symmetric case is also related (in a time-averaged sense) to three-dimensional models that experience small scale convection with no significant large scale shock deformations (e.g., Nordhaus et al. 2010; Wongwathanarat et al. 2010).

Spherically symmetric explosions, arising from boosted neutrino luminosities, involve a transition from a stalled configuration into runaway expansion on timescales longer than the dynamical time. In a realistic setting, the problem is fully time-dependent, and a complete analysis must include the mutual feedback of several effects (e.g., Janka 2001). As a way to facilitate the analysis, Burrows & Goshy (1993) approximated the problem as a steady-state accretion flow, and identified a set of control parameters that determine it. They conjectured that the transition from accretion to explosion involved a global instability of the flow, with an associated critical stability surface in the space of control parameters. State-of-the-art radiation-hydrodynamic simulations show that multidimensional explosions take place at times when the background flow changes slowly (Burrows et al. 2007b; Marek & Janka 2009; Suwa et al. 2010), making a steady-state treatment a reasonable starting point to study dimensionality effects.

Global instabilities of the steady-state flow have been identified in several linear stability studies (Yamasaki & Yamada 2005; Fogliizzo et al. 2007; Yamasaki & Yamada 2007). Using a realistic equation of state (EOS) and weak interactions, Yamasaki & Yamada (2007) found that as the neutrino luminosity is increased, both oscillatory and non-oscillatory modes become unstable. The presence of these modes can be found in spherically-symmetric simulations

<sup>1</sup> Einstein Fellow

dating back to the early days of the delayed neutrino mechanism (e.g., Wilson et al. 1986; Burrows et al. 1995; Buras et al. 2006b; Ohnishi et al. 2006; Murphy & Burrows 2008; Fernández & Thompson 2009a; Nordhaus et al. 2010; Hanke et al. 2011). The instability mechanism behind these modes, their nonlinear development, and their connection to traditional diagnostics for explosion conditions are not completely understood at present, however.

In particular, Burrows & Goshy (1993) found that sequences of steady-state models that satisfy a constraint on the neutrino optical depth are possible only up to a limiting neutrino luminosity, for a given mass accretion rate. This limiting value was found by Murphy & Burrows (2008) to be close to the point where spherically symmetric explosions occur, and by Yamasaki & Yamada (2005) to lie at the critical stability curve in the neutrino luminosity vs. mass accretion rate plane. These results provide support for the assumption that explosion is indeed obtained at the limiting steady-state luminosity (e.g., Pejcha & Thompson 2011). The use of a realistic EOS in the linear analysis yields, however, a flow that becomes unstable for luminosities  $\sim 30\%$  lower than the limiting value, for a specific choice of parameters (Yamasaki & Yamada 2007). Fernández & Thompson (2009a) found, in turn, that unstable modes develop into explosions when parametric microphysics and steady-state boundary conditions are used in time-dependent simulations.

A more widely used diagnostic for explosion is the ratio of the advection to heating time in the gain region (Janka & Keil 1998; Thompson 2000), which is known to have predictive power in the spherically symmetric case (Thompson et al. 2005). If an understanding of the hydrodynamic processes leading to explosion – in any number of dimensions – is to be obtained, then the connection between the limiting steady-state luminosity, stability in spherical symmetry, and proven explosion diagnostics needs to be clarified.

We attempt to shed light on this issue here by studying the properties of unstable modes of the stalled supernova accretion shock, their nonlinear development, and their transition to a runaway solution. Our approach involves time-dependent hydrodynamic simulations, using a realistic EOS and weak interactions. The neutrino radiation field is treated parametrically, as is the fluid accreting onto the stalled shock. We focus on the evolution of the flow in between the neutrinosphere and the shock when the parameters describing this flow are systematically varied. Such a parametric approach has been employed previously to study properties of exploding models and the effects of dimensionality (e.g., Janka & Müller 1996; Ohnishi et al. 2006; Murphy & Burrows 2008).

This paper is organized as follows. Section 2 describes the physical assumptions and numerical methods employed. Section 3 revisits the limiting neutrino luminosity of the steady-state solution and its relation to the neutrino optical depth. Section 4 examines the instability affecting the post-shock flow in the linear and non-linear phase by borrowing analysis tools from stellar pulsation theory. By studying the energetics of the flow, the nature of the instability cycle, approximate stability criteria, and saturation mechanisms are identified. Section 5 probes the validity of the instability criteria over a wide region of parameter space. The influence of numerical resolution, boundary conditions, and other parameters is also investigated. Finally, Section 6 contains a summary of our results and a discussion of the implications for the multi-dimensional case. Readers not interested in technical details

can start in this section, where references to the relevant figures and equations is made.

## 2. METHODS

### 2.1. Physical Model and Approximations

We are interested in hydrodynamic instabilities that mediate the onset of explosion in a stalled core-collapse supernova shock, when the quantities that determine the global character of the accretion flow – mass accretion rate, neutrino luminosity, and protoneutron star radius – begin to evolve slowly relative to the instability timescales<sup>2</sup>. This phase starts around 100 – 200 ms after core bounce (e.g., Liebendörfer et al. 2001). Prior to that, the system is still undergoing transient evolution. Except for progenitors at the lighter mass end (Kitaura et al. 2006; Buras et al. 2006a), simulations with neutrino transport obtain explosions for representative progenitors only after this transient phase is over (Burrows et al. 2007b; Marek & Janka 2009; Suwa et al. 2010).

The background accretion flow then evolves on timescales  $t_{\text{bkg}} \gtrsim 0.1 - 1$  s (e.g., Bethe 1990; Liebendörfer et al. 2001; Buras et al. 2006b). In contrast, the dynamical time, advection time, and thermal time of the flow in between the neutrinosphere and the shock are approximately

$$t_{\text{ff}} \sim 2M_{1.3}^{-1/2} r_7^{3/2} \text{ ms} \quad (1)$$

$$t_{\text{adv}} \sim 10r_7v_{r,9}^{-1} \text{ ms} \quad (2)$$

$$t_{\text{th}} \sim 20M_{1.3}r_7^{-1}Q_{\text{net},21}^{-1} \text{ ms}, \quad (3)$$

where  $M_{1.3}$  is the mass enclosed within the shock in units of  $1.3M_{\odot}$ ,  $r_7$  is the radial distance from the center of mass in units of  $10^7$  cm,  $v_{r,9}$  the radial velocity in units of  $10^9$  cm s<sup>-1</sup>, and  $Q_{\text{net},21}$  the net specific neutrino energy source term, in units of  $10^{21}$  erg g<sup>-1</sup> s<sup>-1</sup> ( $\sim 1$  GeV per baryon). These timescales are usually shorter than  $t_{\text{bkg}}$  by a factor of at least several, making a steady-state model a reasonable background state to study global hydrodynamic instabilities and the transition to explosion (Burrows & Goshy 1993).

In this study we adopt a parametric approach in that we do not compute the neutrino radiation field and boundary conditions starting from a stellar progenitor. Instead, we regard the quantities determining those processes as free parameters, and study the behavior of the system as these parameters are varied. This approach has previously been used by a number of authors to study the hydrodynamic response of the stalled accretion shock (e.g., Blondin et al. 2003; Ohnishi et al. 2006; Murphy & Burrows 2008; Iwakami et al. 2008; Fernández & Thompson 2009a; Nordhaus et al. 2010; Hanke et al. 2011).

In our model, we ignore the interior of the protoneutron star, as we are interested in the dynamics of the fluid between the neutrinosphere and the shock. Instead, we establish a spherical inner boundary at the radius of the forming neutron star. A time-independent neutrino flux is imposed at this surface. We consider only electron-type neutrinos and antineutrinos, as these are the only species that exchange energy with matter with a significant cross-section (e.g., Bethe 1990). For simplicity, we establish a single neutrinosphere at a time-independent radius  $R_{\nu}$ , and assume that neutrinos stream isotropically from this surface. In a more realistic

<sup>2</sup> The mass of the protoneutron star is another fundamental parameter of the flow, but it must vary slowly in neutron-star-forming supernovae.

treatment, the difference between the energy averaged electron neutrino- and antineutrinosphere radius is of the order of 10% (e.g., Buras et al. 2006b).

Both neutrino species are assumed to have a Fermi-Dirac spectrum with zero chemical potential. To remain close to results from more detailed radiation-hydrodynamic simulations, we set the neutrino luminosities of both species to be equal, but allow them to have different neutrinospheric temperatures (e.g., Janka 2001). This is achieved by allowing the normalization of the neutrino luminosity to vary freely relative to the neutrinospheric temperature and radius (Appendix A).

The contribution to neutrino heating from the accretion luminosity is not included explicitly. To first approximation, the amount of heating required to start an explosion depends only on the total flux incident on the gain region, which lies above the cooling region, so both contributions can be absorbed by the core luminosity in steady-state. However, instability of the post-shock flow generates changes in the mass accretion rate, hence a non-trivial feedback from the accretion luminosity can alter the stability properties. We discuss the implications of this approximation in §4.5.

The mass accretion rate is taken to be constant in time. Only the point-mass gravity of the protoneutron star is considered, as the self-gravity of the envelope is a  $\lesssim 10\%$  correction to the dynamics. This gravitating mass remains constant in time.

Starting from a steady-state accretion flow defined as above, we evolve the system for different values of the control parameters that set the background solution. In particular, we study the evolution of sequences of models with different neutrino luminosities, for fixed values of the mass accretion rate and neutrinospheric radius. Our goal is to identify the hydrodynamic processes by which a quasi-steady state configuration transitions into an exploding solution, and to determine the conditions (quantified by the control parameters) for which this transition occurs.

## 2.2. Equations and Coordinate System

Spherical symmetry is assumed throughout this paper, with the origin at the center of the protoneutron star. The time-dependent system is described by the equations of mass, momentum, energy, and lepton number conservation in spherical polar coordinates, with source terms due to the gravity of a point mass  $M$  and charged-current weak interactions:

$$\frac{\partial \rho}{\partial t} + \frac{1}{r^2} \frac{\partial}{\partial r} (r^2 \rho v_r) = 0 \quad (4)$$

$$\frac{\partial v_r}{\partial t} + v_r \frac{\partial v_r}{\partial r} + \frac{1}{\rho} \frac{\partial p}{\partial r} + \frac{GM}{r^2} = 0 \quad (5)$$

$$\frac{\partial(\rho e)}{\partial t} + \frac{1}{r^2} \frac{\partial}{\partial r} (v_r [\rho e + p]) + \rho v_r \frac{GM}{r^2} = \mathcal{L}_{\text{net}} \quad (6)$$

$$\frac{\partial Y_e}{\partial t} + v_r \frac{\partial Y_e}{\partial r} = \Gamma_{\text{net}} \quad (7)$$

We denote respectively by  $\rho$ ,  $v_r$ ,  $p$ ,  $G$ ,  $e$ , and  $Y_e$ , the mass density, radial velocity, total pressure, gravitational constant, specific energy, and electron fraction. Source terms due to weak interactions are calculated in tabular form, with details provided in Appendix A. The relevant contributions are the net rate of heating minus cooling per unit volume  $\mathcal{L}_{\text{net}}$ , and the net rate per baryon of electron minus positron generation  $\Gamma_{\text{net}}$ .

The system of equations (4)-(7) is closed with an EOS that yields the relation  $p(\rho, e_{\text{int}}, Y_e)$ , with  $e_{\text{int}} = e - v_r^2/2$  the specific

internal energy. We use the model of Shen et al. (1998), as implemented by O'Connor & Ott (2010)<sup>3</sup>. The high-density part of EOS does not make a significant difference at the densities considered here,  $\rho \lesssim 10^{11} \text{ g cm}^{-3}$ . The important components are nucleons, alpha particles, and heavy nuclei in nuclear statistical equilibrium, supplemented by photons and electron-positron pairs with an arbitrary degree of degeneracy and relativity.

## 2.3. Initial Conditions

The initial condition for time-dependent simulations consists of a steady-state spherical accretion flow with a shock at some radial distance  $R_s$  from the center, obtained by solving equations (4)-(7) without time derivatives. Solutions upstream and downstream of the shock are connected through the Rankine-Hugoniot jump conditions (e.g., Landau & Lifshitz 1987).

Conditions upstream of the shock are determined by requiring that the velocity, entropy, and electron fraction of the supersonic flow have specified values at a fixed radial coordinate  $r_{\text{vf}}$ . In order to obtain values that are in close agreement with more realistic one-dimensional simulations (e.g., Liebendörfer et al. 2001; Buras et al. 2006b), we set  $r_{\text{vf}} = 100 \text{ km}$  for all simulations. At this radius, we set the radial velocity to the local free-fall velocity, the entropy per baryon to  $5k_B$ , and the electron fraction to  $1/2$ . These parameters together with the mass accretion rate  $\dot{M}$ , the gravitating mass  $M$ , and the shock radius  $R_s$  yield the mass density, internal energy, electron fraction, and velocity upstream of the shock, by integrating the steady-state equations from  $r_{\text{vf}}$  to  $R_s$ . The sensitivity of our results to these choices is examined in §5.2.

For a given set of parameters, the shock radius  $R_s$  is obtained by iteratively solving for the downstream flow from a trial shock position to  $R_\nu$ , until an additional constraint is satisfied. Following previous studies of steady-state core-collapse supernova flows (e.g., Burrows & Goshy 1993; Yamasaki & Yamada 2005, 2006, 2007; Pejcha & Thompson 2011), this additional closure relation is obtained by requiring that the neutrino optical depth from  $R_\nu$  to the shock

$$\tau_\nu = \int_{R_\nu}^{R_s} \kappa_\nu dr \quad (8)$$

is equal to  $2/3$ . By default, we set  $\kappa_\nu$  to the effective absorption coefficient of electron-type neutrinos  $\kappa_{\text{eff}} = \sqrt{\kappa_{\text{abs}}(\kappa_{\text{sc}} + \kappa_{\text{abs}})}$  (Janka 2001), where

$$\kappa_{\text{abs}} \simeq 1.96 \times 10^{-7} T_{\nu e,4}^2 \rho_{10} Y_n \text{ cm}^{-1} \quad (9)$$

corresponds to charged-current absorption and

$$\kappa_{\text{sc}} \simeq 0.51 \times 10^{-7} T_{\nu e,4}^2 \rho_{10} (Y_n + Y_p) \text{ cm}^{-1} \quad (10)$$

to elastic scattering with nucleons, to lowest order in the neutron-proton mass difference over the neutrino energy (e.g., Bruenn 1985). In equations (9)-(10),  $T_{\nu e,4}$  is the electron neutrinospheric temperature in units of 4 MeV,  $\rho_{10}$  the mass density in units of  $10^{10} \text{ g cm}^{-3}$ , and  $\{Y_n, Y_p\}$  the number of neutrons and protons per baryon, respectively. To test the sensitivity of our results to this prescription for the optical depth, we also compute solutions with pure absorption ( $\kappa_\nu = \kappa_{\text{abs}}$ ),

<sup>3</sup> Available at <http://stellarcollapse.org>.

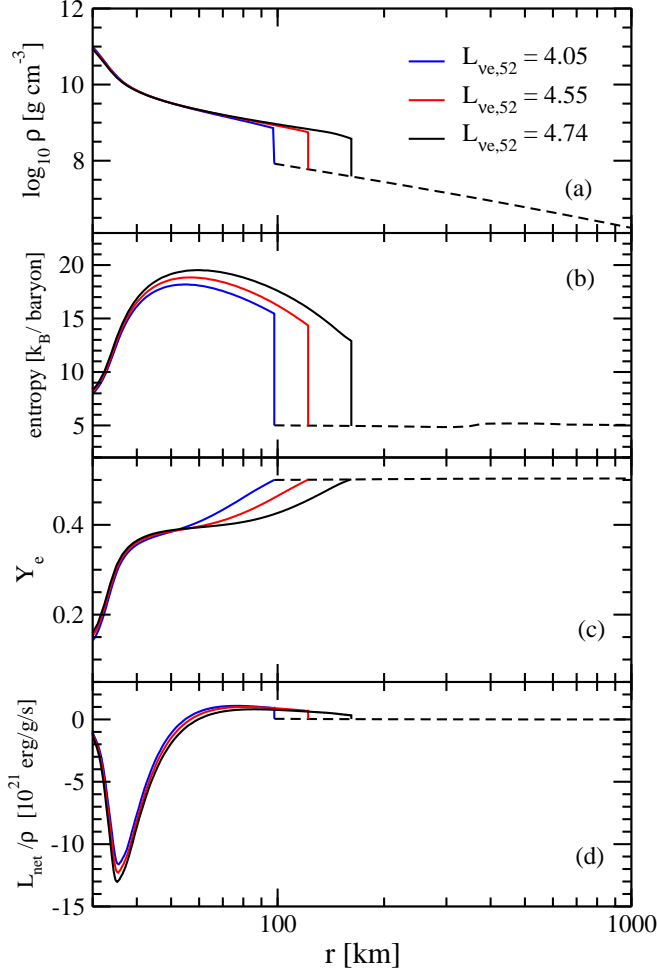


FIG. 1.— Initial profiles of density (a), entropy (b), electron fraction (c), and net neutrino energy generation rate  $\mathcal{L}_{\text{net}}/\rho$  (d) as a function of radius, obtained by solving the steady-state version of equations (4)-(7) as described in §2.3. Parameters correspond to our fiducial sequence (§2.5). Curves shown correspond to neutrino luminosities at the approximate instability thresholds for oscillatory modes (blue) and non-oscillatory modes (red), plus the limiting luminosity for a steady-state solution (black).

or total absorption plus scattering ( $\kappa_\nu = \kappa_{\text{abs}} + \kappa_{\text{sc}}$ ), thereby bracketing our default choice (§5.2).

Figure 1 shows characteristic radial profiles of density, entropy, electron fraction, and net specific neutrino energy generation rate for a few neutrino luminosities, given  $M = 0.3M_\odot \text{ s}^{-1}$  and  $R_\nu = 30 \text{ km}$ .

#### 2.4. Time-dependent Implementation

We use FLASH3.2 (Dubey et al. 2009) to evolve the system of equations (4)-(7). The public version of the code has been modified to include the EOS implementation of O’Connor & Ott (2010), weak interaction rates, and a grid of variable spacing. Details about the latter are provided in Appendix B.

We locate the inner simulation boundary at the neutrospheric radius  $R_\nu$ . The outer boundary  $r_{\text{max}}$  is chosen to be 1000 km for most models, corresponding to approximately four times the radius where the nuclear binding energy of alpha particles equals their gravitational binding energy,

$$r_\alpha = 254 \left( \frac{M_{\text{enc}}}{1.3M_\odot} \right) \text{ km}, \quad (11)$$

where  $M_{\text{enc}}$  is the mass enclosed at a radius  $r_\alpha$ . Above this radius, the shock accelerates significantly during an explosion (e.g., Fernández & Thompson 2009a and §4.4).

We use two types of boundary condition at  $R_\nu$ . Our default implementation fixes all variables in the ghost cells to their initial values, obtained by continuing the steady-state solution inside  $R_\nu$ . This prescription fixes the mass-, momentum-, and energy fluxes leaving the domain. A truly reflecting boundary condition would cause the shock to drift outwards with time due to the accumulation of mass around  $R_\nu$ , because the latter does not recede (as it would do with a more realistic treatment, e.g., Scheck et al. 2006). Fernández & Thompson (2009b) and Fernández & Thompson (2009a) were able to use a reflecting boundary condition with a fixed neutrospheric radius because their parametric cooling function was very centrally concentrated, resulting in accumulation of mass in a few cells outside  $R_\nu$ , and thus eliminating the shock drift effect. The cooling function used here has, in contrast, a shallower radial dependence.

To test the influence of the default inner boundary condition on our results, we also run a few models that allow an arbitrary amount of mass to leave the domain, while still providing pressure support to the accretion flow. The density and radial velocity in the ghost cells inside  $R_\nu$  are set to

$$\rho(r) = \rho_0(r) + \rho(r_1) - \rho_0(r_1) \quad (12)$$

$$v_r(r) = \left( \frac{r_1}{r} \right)^2 v_r(r_1), \quad (13)$$

where  $r$  is the radial position of a given ghost cell,  $r_1$  corresponds to the center of the first active cell outside the inner boundary, and the subscript zero labels the initial steady-state solution. All other variables are set to have zero gradient and are thus copied from the innermost active cell into the ghost cells. The additional factor multiplying the velocity accounts for the radial convergence of the flow (Ohnishi et al. 2006).

The radial cell spacing  $\Delta r$  is ratioed (as in, e.g., Stone & Norman 1992):  $\Delta r_{i+1}/\Delta r_i = \zeta$ , with  $i$  denoting cell number and  $\zeta$  some positive real number greater than one. We space our cells logarithmically, with  $\zeta = (r_{\text{max}}/R_\nu)^{N_r}$ , where  $N_r$  is the total number of cells, and the size of the cell closest to the inner boundary  $\Delta r_{\text{min}} = R_\nu(\zeta - 1)$  (Appendix B). Guided by convergence tests, we choose either 880 or 1760 cells for our runs, although some models are evolved at resolutions up to  $N_r = 3200$  (§5.2). The corresponding values of  $(\zeta - 1)$  are 0.4%, 0.2%, and 0.1%, respectively, for  $r_{\text{max}} = 1000 \text{ km}$  and  $R_\nu = 30 \text{ km}$ .

To avoid problems with the Riemann solver whenever the internal energy becomes negative, we implement the prescription of Buras et al. (2006b), adding the nuclear binding energy of alpha particles, heavy nuclei, and the rest mass energy of electrons to the internal energy during the hydrodynamic step. The mass fractions of alpha particles and heavy nuclei are then advected as passive scalars in between calls to the equation of state. In some cases where the Mach number of the upstream flow is  $\gtrsim 5$ , we add an additional zero point of  $7 \times 10^{17} \text{ erg g}^{-1}$  to prevent the internal energy to be negative at large radii. This constant shift makes a negligible difference in the evolution of the shock.

To prevent the system from reaching the lower limit on  $Y_e$  allowed by the equation of state implementation, and to account for the decrease in neutrino flux around the neutrosphere in a very crude manner, we multiply all the neutrino

TABLE 1  
 MODEL SEQUENCES EVOLVED

$R_\nu$	$\dot{M}$ ( $M_\odot \text{ s}^{-1}$ )	$L_{\nu_e}$ ( $10^{52} \text{ erg s}^{-1}$ )	$N_r$
20 km	0.1-0.5	2.0 - 14.0	1760
30 km	0.1-1	1.5 - 13.7	880
40 km	0.1-1	1.0 - 8.9	880
$\propto L_{\nu_e}^{1/2}$	0.1-1	1.0 - 5.5	880
30 km	0.3	3.8 - 4.6	240-3200

source terms by a suppression factor

$$f_{\text{sup}}(\rho) = e^{-(\rho/\rho_0)} \quad (14)$$

where  $\rho_0 = 10^{11} \text{ g cm}^{-3}$  is a fiducial density, chosen so as to match the characteristic density at the neutrinosphere. Given that the effective neutrino optical depth depends chiefly on density (eq. [8]), the factor in equation (14) amounts to a reduction  $\sim e^{-\tau_\nu}$  (e.g., Murphy & Burrows 2008). The choice of  $\rho_0$  has some mild influence on the threshold for instability, but it doesn't significantly affect the relative differences between models (§5.2).

A small initial transient is produced in the form of an outgoing sound wave from the inner boundary and downgoing entropy and sound waves from the shock. The former acts as an initial perturbation.

### 2.5. Models Evolved

We evolve sequences of models with varying neutrino luminosity  $L_{\nu_e}$  ( $= L_{\bar{\nu}_e}$ ), for a given mass accretion rate  $\dot{M}$  and prescription for the neutrinospheric radius  $R_\nu$ . Our *fiducial sequence* corresponds to  $\dot{M} = 0.3M_\odot \text{ s}^{-1}$  and  $R_\nu = 30 \text{ km}$ , with other parameters fixed to values as described in §2.3. This default sequence closely resembles the flow obtained at late times in the evolution of a  $15M_\odot$  progenitor (e.g., Liebendörfer et al. 2001; Marek & Janka 2009).

We explore a wider region of parameter space with a grid of constant  $R_\nu$  and  $\dot{M}$  sequences such that  $R_\nu = \{20, 30, 40\} \text{ km}$  and  $\dot{M} = \{0.1, 0.3, 0.5, 0.75, 1\} M_\odot \text{ s}^{-1}$ , with our fiducial sequence as one of its members. We add another sequence, following Burrows & Goshy (1993), that relates the neutrinospheric radius to the neutrino luminosity through the Fermi-Dirac distribution at constant neutrinospheric temperature and zero chemical potential (equation [A3] with  $N_{\nu_e} = 1$ ), namely  $R_\nu \propto L_{\nu_e}^{1/2}$ . In this case we use the same grid in  $\dot{M}$  as in the constant  $R_\nu$  models. All sequences are summarized in Table 1.

### 3. ON THE LIMITING NEUTRINO LUMINOSITY OF THE STEADY-STATE SOLUTION

Burrows & Goshy (1993) found that steady-state solutions to the accretion shock problem in the supernova context can exist only up to a maximum value of the neutrino luminosity (the *Burrows-Goshy limit* hereafter). Recently, Pejcha & Thompson (2011) have related this limit to a critical value of the ratio of sound speed to free-fall speed in the postshock region, in analogy with isothermal accretion flows. Here we provide an alternative (but equivalent) explanation.

The existence of a limiting neutrino luminosity for the steady-state solution is related to the requirement that the neutrino optical depth have a fixed value (eq. [8]). This closure relation is used for self-consistency with the assumed neutrino radiation field, but has no significance from the purely hydro-

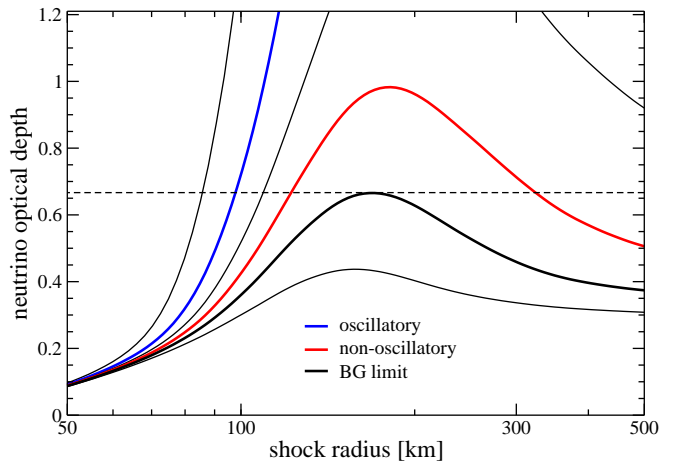


FIG. 2.— Neutrino optical depth  $\tau_\nu$  (eq. [8]) as a function of shock radius  $R_s$ , for parameters corresponding to our fiducial sequence of models (§2.5). Each curve is obtained by fixing the neutrino luminosity and integrating the time-independent version of equations (4)-(7) from an arbitrary shock position to  $R_\nu$ , keeping the upstream flow fixed. Curves with decreasing amplitude correspond to electron neutrino luminosities  $L_{\nu_e} = \{3.5, 4.05, 4.35, 4.55, 4.74, 5\} \times 10^{52} \text{ erg s}^{-1}$ , respectively. The thick blue and red curves correspond to the approximate instability threshold for oscillatory and non-oscillatory modes, respectively (§4.3). Solutions consistent with neutrino radiation transport correspond to the intersection of each curve with the  $\tau_\nu = 2/3$  dashed line. The Burrows-Goshy limit is marked by a thick black curve that has a maximum at exactly  $2/3$ . The effective optical depth for electron-type neutrinos is used to compute  $\tau_\nu$  (§2.3).

dynamic point of view<sup>4</sup>. By relaxing this constraint, one can examine the behavior of  $\tau_\nu$  as a function of shock radius and neutrino luminosity, in order to gain insight into the processes that determine this limit.

Figure 2 shows the neutrino optical depth  $\tau_\nu$  as a function of shock radius  $R_s$  at  $t = 0$  for several neutrino luminosities in our fiducial sequence. Each point along a given curve is obtained by integrating the steady-state version of equations (4)-(7) from an arbitrary shock position down to a constant  $R_\nu$ , keeping the upstream flow fixed, and calculating equation (8). For small shock radii, the optical depth is a monotonically increasing function of  $R_s$ . For large enough shock radii, however,  $\tau_\nu(R_s)$  reaches a maximum and then decreases for increasing  $R_s$ . Larger neutrino luminosities move this maximum towards smaller shock radii and decrease its magnitude. The two points where this curve reaches a value of  $2/3$  correspond to the two physical solutions found by Yamasaki & Yamada (2005) and Pejcha & Thompson (2011). Further increases in the neutrino luminosity cause the maximum of  $\tau_\nu$  to fall below  $2/3$ , making it impossible to satisfy the optical depth constraint.

The function  $\partial\tau_\nu/\partial R_s$  has two contributions. The first comes from the increase in the volume of the postshock region and is always positive for fixed  $R_\nu$ . The second arises from a change in the quantities that determine  $\kappa_\nu$ , chiefly the density profile (eqns. [9]-[10]), and can have either sign. Figure 3a shows the density profile of the model at the Burrows-Goshy limit and another with neutrino luminosity 5% larger and the same shock radius (corresponding to the lowest solid curve in Figure 2). The density of the higher luminosity configuration is lower by a factor of the order of 2 near the neutrinosphere, where the bulk of the optical depth is generated.

The density decrease in the cooling layer is caused by an

<sup>4</sup> The settling of a shocked accretion flow onto a spherical surface with an arbitrary heating and cooling function is a well-defined hydrodynamic problem, albeit not necessarily realistic.

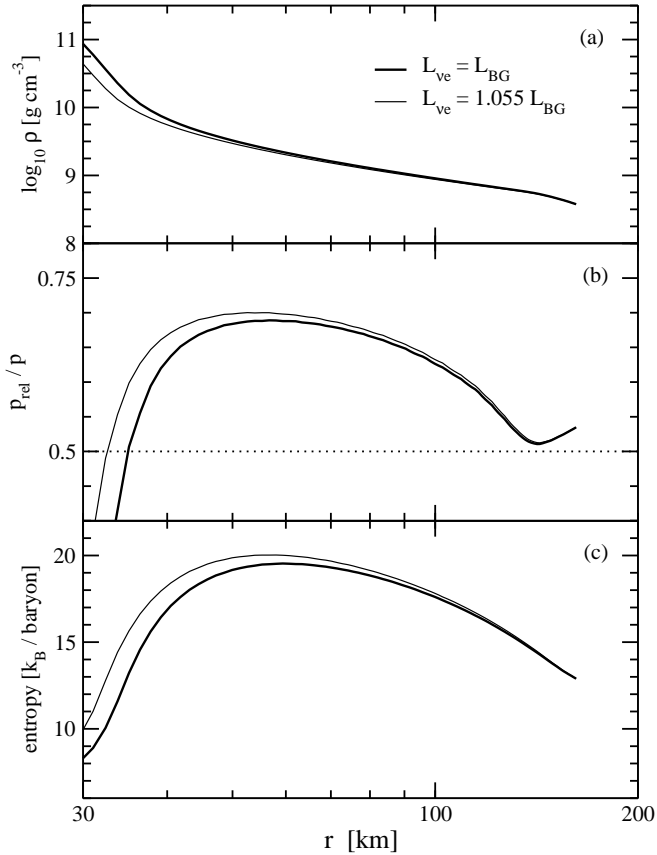


FIG. 3.— Profiles of density (a), ratio of pressure in leptons and radiation to total pressure (b), and entropy (c) for two models from our fiducial sequence which have the same shock radius but different neutrino luminosities. The thick line corresponds to the Burrows-Goshy limit, while the thin line has a neutrino luminosity 5% higher. A higher entropy in the gain region increases the fraction of the total pressure provided by relativistic particles at fixed radius, softening the density profile and thus decreasing the density around the neutrinosphere. This is the reason why the lowest curve in Figure 2 falls below  $\tau_\nu = 2/3$ .

inward motion of the radius at which the pressure transitions from being dominated by leptons and radiation to being set by non-relativistic nucleons. This is shown by Figure 3b. The adiabatic index in the relativistic particle dominated region is closer to  $4/3$ , while nucleon domination moves it towards  $5/3$ , causing a steepening of the density profile at this transition<sup>5</sup>. Inward motion of the transition region relative to  $R_\nu$  causes the density to be lower at this radius. The change in the transition radius in turn is caused by a higher entropy in the gain region (Figure 3c), which increases the contribution from relativistic particles. Finally, the higher entropy is the result of the higher heating rate arising from the higher neutrino luminosity.

In the case where the neutrinospheric radius is tied to the neutrino luminosity at constant temperature (e.g., Burrows & Goshy 1993, Yamasaki & Yamada 2007), an additional contribution arises from the change of the lower limit of integration in equation (8). This decreases the size of the integration volume for increasing neutrino luminosity relative

<sup>5</sup> The steepening of the density profile with a higher adiabatic index occurs because the temperature varies slowly with radius near the neutrinosphere. The pressure gradient needed to balance gravity thus arises mostly from the density gradient. In contrast, in the  $\gamma \simeq 4/3$  region the pressure gradient arises mostly from the changes in the temperature, with the density profile being thus shallower (Janka 2001).

to the case where  $R_\nu$  is constant, making  $\tau_\nu$  smaller than it would otherwise be.

Pejcha & Thompson (2011) found that the Burrows-Goshy limit can be characterized by a critical value of the ratio of the sound speed to free-fall speed at some point in the flow, above which it is not possible to connect a subsonic settling solution to a supersonic accretion flow via the hydrodynamic shock jump conditions (see also Yamasaki & Yamada 2005). Implicit in this result, however, is the simultaneous fulfillment of the boundary conditions at the upstream side of the shock and at the neutrinosphere when constructing the two solutions. Here we have adopted a uni-directional approach, keeping only the upstream boundary condition and integrating the fluid equations inward until an additional constraint is met at the base. This allows us to violate the optical depth condition by varying the shock position, which can be placed at any point in the upstream solution. The conclusions of both approaches regarding the nature of the Burrows-Goshy limit are equivalent when viewed in this light, as a higher sound speed relative to the free-fall velocity implies higher entropy (see Murphy & Meakin 2011 for a discussion of the connection between these two quantities through the entropy equation).

#### 4. TRANSITION TO RUNAWAY EXPANSION

In this section we analyze the instabilities that mediate the transition to runaway expansion, using simulation results and adapting analysis techniques from stellar pulsation theory. The term *explosion* implies the existence of a star whose envelope is to be ejected by a successful shock. Given the parametric character of our study, we employ instead the term *runaway expansion* to denote the *onset* of explosion in a medium with constant mass accretion rate, as the asymptotic explosion energy is determined by additional processes not included here (e.g., Marek & Janka 2009).

Evolving any of the model sequences described in §2.5 yields a characteristic outcome for the evolution of the shock radius as a function of time. The result for selected models from our fiducial sequence is shown in Figure 4. Models with low neutrino luminosity are stable to small perturbations. For  $4.05 < L_{\nu_e}/(10^{52} \text{ erg s}^{-1}) < 4.55$ , the shock undergoes oscillations of growing amplitude that transition to runaway expansion after some time delay. For  $L_{\nu_e} > 4.55 \times 10^{52} \text{ erg s}^{-1}$ , initial exponential growth in amplitude occurs without any oscillation, transitioning into a nearly constant-velocity expansion phase at later times.

The characteristic timescale associated with both types of modes is the advection time from the shock to the protoneutron star

$$t_{\text{adv}} = \int_{R_\nu}^{R_s} \frac{dr}{|v_r|} = \frac{M_{\text{env}}}{\dot{M}}, \quad (15)$$

where the second equality is valid when  $\dot{M}$  is constant, and  $M_{\text{env}}$  is the mass enclosed between the neutrinospheric radius and the shock. The fluid velocity is very subsonic, hence the kinetic energy content is small. Changes in the accretion flow involve changes in the heat content of the fluid through modulation of the neutrino emission and absorption processes, hence the instabilities involved are non-adiabatic.

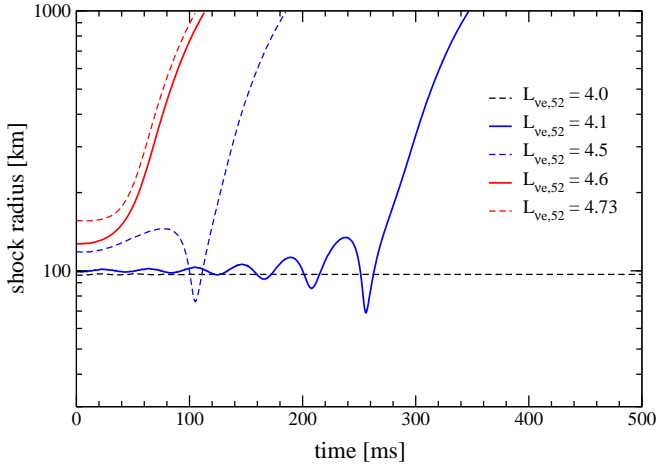


FIG. 4.— Shock radius as a function of time for selected models from our fiducial sequence. Different curves correspond to different electron neutrino luminosities as labeled ( $L_{\nu_e,52} = L_{\nu_e}/10^{52}$  erg  $s^{-1}$ ). Stable, oscillatory, and non-oscillatory modes are plotted as black, blue, and red curves, respectively. The maximum luminosity for a steady-state solution at fixed optical depth (the Burrows-Goshy limit, §3) corresponds to  $L_{\nu_e,52} \simeq 4.74$  for this set of parameters.

#### 4.1. Work Integral for Accretion Shocks

Any instability involves the conversion of energy from one type to another as the system transitions into a more favorable configuration. In stellar pulsation theory, the standard tool used to quantify this conversion is the *work integral* (Eddington 1926; Unno et al. 1989), which is defined as the change in the total energy  $E$  of the system over an oscillation cycle

$$W = \oint dt \frac{dE}{dt}. \quad (16)$$

In pulsating stars, the total mass of the system is essentially constant within an oscillation period, thus equation (16) is normally written to consider Lagrangian changes (e.g., Unno et al. 1989)<sup>6</sup>.

In contrast, for an accretion shock neither the mass nor the volume enclosed within the star and the shock remain constant in time, hence an Eulerian expression must be used if one wants to adapt this tool to the problem at hand. Writing the total specific energy as

$$e_{\text{tot}} = e - \frac{GM}{r}, \quad (17)$$

and rearranging the gravitational contribution to equation (6), the Eulerian rate of change of the total energy in spherical symmetry becomes

$$\frac{\partial E}{\partial t} = \int d^3x \frac{\partial(\rho e_{\text{tot}})}{\partial t} + 4\pi R_s^2 \dot{R}_s (\rho e_{\text{tot}})|_{R_s} \equiv \dot{E}_{\text{tot}} \quad (18)$$

$$= \dot{E}_{\text{N}} - \dot{E}_{\text{up}} + \dot{E}_{\text{dn}} + \dot{E}_s, \quad (19)$$

with

$$\dot{E}_{\text{N}} = \int_{R_{\text{in}}}^{R_s} 4\pi r^2 dr \mathcal{L}_{\text{net}} \quad (20)$$

$$\dot{E}_{\text{up}} = 4\pi R_s^2 [v_r(\rho e_{\text{tot}} + p)]|_{R_s} \quad (21)$$

<sup>6</sup> The work integral for stars is also simplified by the pressure falling to very small values at the surface, which is not the case for flow confined by an accretion shock.

$$\dot{E}_{\text{dn}} = 4\pi R_{\text{in}}^2 [v_r(\rho e_{\text{tot}} + p)]|_{R_{\text{in}}} \quad (22)$$

$$\dot{E}_s = 4\pi R_s^2 \dot{R}_s (\rho e_{\text{tot}})|_{R_s}, \quad (23)$$

where  $\dot{R}_s$  denotes the rate of change of the shock position, and  $R_{\text{in}}$  is some inner boundary that remains fixed. Equations (18)-(23) can be straightforwardly extended to allow for a moving inner boundary and non-trivial integration over angles. An analogous expression was derived by Janka (2001) to study the evolution of the mass and energy in the gain region.

The first three terms in equation (19) represent, respectively, the integrated neutrino source terms plus the energy fluxes entering and leaving the integration domain with the accretion flow. In steady-state, these three terms cancel out exactly. The fourth term is non-zero only when the shock moves, and accounts for the change in energy caused by a change in the postshock-volume. Because the total specific energy just below the shock is generally negative due to dissociation losses, this term provides damping on expansion and driving on contraction.

Because the evolution of the shocked flow is not necessarily periodic, we will make use of equation (18) rather than (16) to track the different energetic components in the system. Also, given that the entire flow between  $R_{\nu}$  and  $R_s$  is in sonic contact, analysis of global instabilities must include the cooling region, thus we will take  $R_{\text{in}}$  as close as possible to  $R_{\nu}$ . Details about the calculation of equations (18)-(23) from our simulations are provided in Appendix C.

#### 4.2. Linear Phase: Oscillatory and Non-Oscillatory Modes

Figure 5 shows the evolution of the shock radius and the different terms that account for change of the total energy (eq. [19]), for a model that explodes via an oscillatory mode ( $L_{\nu_e,52} = 4.1$ ). The lower integration boundary  $R_{\text{in}}$  was chosen to be a few cells above  $R_{\nu}$ , to eliminate boundary effects (Appendix C).

In the linear phase, the magnitude of the energy generation by shock motion  $\dot{E}_s$  peaks when the shock velocity is the largest, and is dominated by the gravitational term in  $e_{\text{tot}}$ . Contractions thus inject positive energy into the postshock region. The net energy generation from accretion  $\dot{E}_{\text{N}} - \dot{E}_{\text{up}} + \dot{E}_{\text{dn}}$  also becomes non-zero once the system deviates from equilibrium. Its magnitude is much smaller than the individual terms that comprise it, showing that imperfect cancellation between the energy fluxes and neutrino source terms is the additional source of energy. The lowest panel in Figure 5 shows that in fact the flow adjusts itself in the linear phase to match the energy generation from shock motion with the excess energy flux entering the domain,  $\dot{E}_s(t) \simeq \dot{E}_{\text{up}}(t) - \dot{E}_{\text{up}}(0)$ . The total energy generation can then be accounted for entirely by the deviation from steady-state of the neutrino source terms and the energy flux leaving the domain toward the protoneutron star. In other words, oscillatory instability arises from a mismatch in the dissipation of the accretion energy in a system with a moving boundary.

The origin of this imbalance can be traced back to the steep temperature dependence of the neutrino cooling function,  $\mathcal{L}_c/\rho \propto T^6$  (eq. [A13]). Figure 6 shows that the perturbation to the specific neutrino source term closely mirrors the temperature perturbation, with the opposite sign (after removing the density dependence, the heating term depends only on the neutron and proton abundance, linearly). Thus an increase in the temperature from its steady-state value causes an increase in the rate of cooling and hence excess energy dissipa-

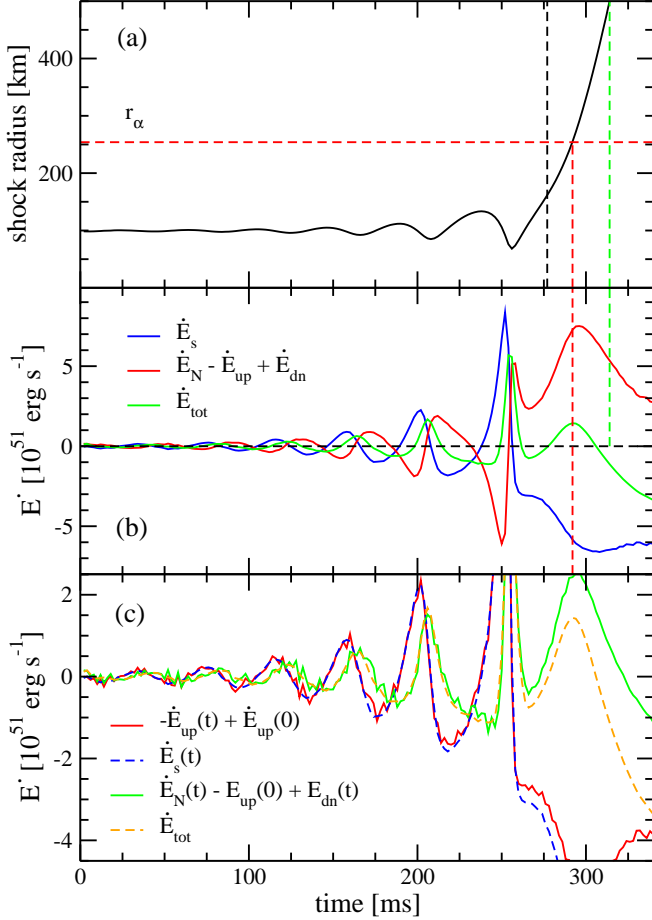


FIG. 5.— Evolution of the different rates of energy change (eq. [19]) for a model in our fiducial sequence which explodes via oscillatory instability ( $L_{\nu_e,52} = 4.1$ ). Panel (a) shows the shock radius as a function of time (solid black), and the radius at which the binding energy of alpha particles equals their gravitational binding energy (eq. [11], horizontal red dashed). The vertical dashed black line signals the time at which the fluid achieves positive total energy for the first time (see also Fig. 9), while the green dashed line shows the time at which the sound crossing time from the shock to  $R_\nu$  becomes longer than the shock expansion time  $R_s/v_s$ . Panel (b) shows the energy generation due to shock motion (blue), the net energy generation from accretion (red), and the total rate of change of energy (green). Panel (c) shows the fluctuation (relative to the initial condition) in the energy flux entering through the shock (solid red), the energy generation from shock motion (dashed blue), the fluctuation in the energy flux leaving the domain minus neutrino cooling (solid green), and the total rate of change of energy (dashed orange). Note that the vertical scale changes relative to panel (b).

tion. This results in contraction and cooling of the postshock volume on a sound crossing time, reversing the cycle when the lower temperature fluid reaches the cooling region by advection.

Figure 6 also shows that the period of the oscillation is related to the advection time from the shock to a radius near the point of maximum cooling. At this radius the flow achieves maximum deceleration, and advected perturbations are efficiently converted into acoustic waves (Scheck et al. 2008; Foglizzo 2009; Sato et al. 2009). The normalized density perturbation is significant only outside of this radius, below which it undergoes a phase shift. The model shown in Figure 6 has a period very close to twice the advection timescale from the shock to this radius. This is very close to the period of an oscillatory mode with no heating (Fernández & Thompson 2009b). As the flow becomes unstable, however, the oscillation period becomes increasingly

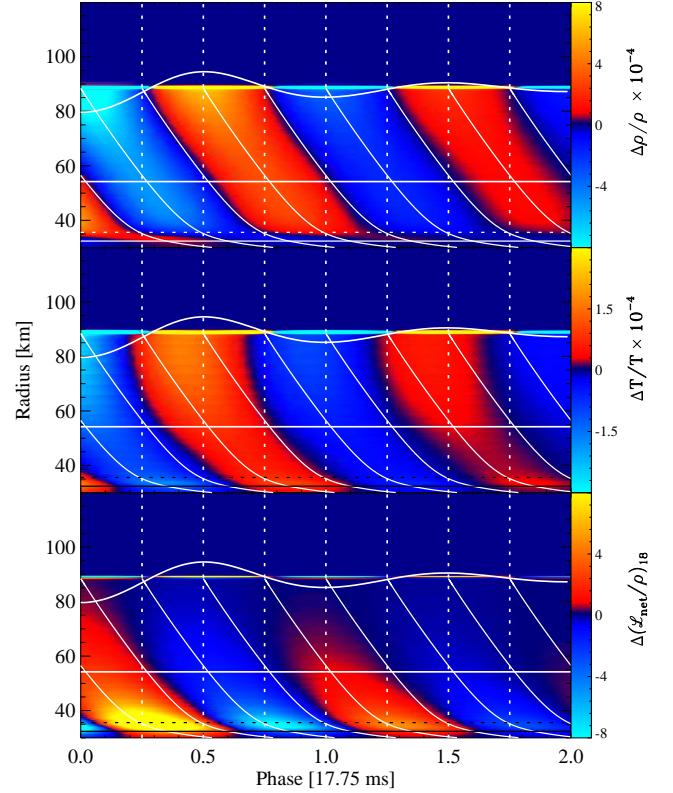


FIG. 6.— Spacetime diagram showing different perturbed quantities as a function of time for a stable model in our fiducial sequence ( $L_{\nu_e,52} = 3.5$ ). Two complete oscillation cycles are shown, and the differences are taken relative to values at very late times, where the flow reaches perfect steady-state. The top panel shows normalized density fluctuations, the middle normalized temperature fluctuations, and the bottom the fluctuation in the specific net neutrino source term  $\mathcal{L}_{\text{net}}/\rho$  in units of  $10^{18} \text{ erg g s}^{-1}$ . Horizontal lines correspond to the gain radius (upper solid white), maximum cooling (dashed black/white), and radius where cooling has decreased by an e-folding from its maximum (white/black solid near bottom of each panel). Diagonal lines correspond to streak lines in the unperturbed solution. The amplitude of the shock radius (white wavy curves) has been increased by a factor of 100 for clarity.

longer, achieving nearly four advection times at the threshold for oscillatory instability. This lengthening of the oscillation period with neutrino luminosity has been attributed to buoyancy effects by Yamasaki & Yamada (2007).

Non-oscillatory modes grow exponentially in amplitude and transition directly into runaway expansion. The different terms that make up the rate of change of total energy are shown in Figure 7 (the model has  $L_{\nu_e,52} = 4.6$ ). The evolution of these terms resembles the last expansion phase of oscillatory modes, where the shock motion term acts only as a sink of energy and is not matched by the deviation in  $\dot{E}_{\text{up}}$  from steady-state. The expansion is driven by the net energy generation from accretion, which is positive throughout.

### 4.3. Approximate Instability Criteria

The only way to obtain an exact instability threshold for these non-adiabatic modes is to perform a linear perturbation analysis of equations (4)-(7) such as that done by Yamasaki & Yamada (2007). In the absence of such a calculation, we have instead searched for physically motivated instability criteria that correctly describe the behavior of our simulations over a wide range of parameter space. We discuss here their definition, and leave for §5 their comparison with simulations over an extended region of parameter space.

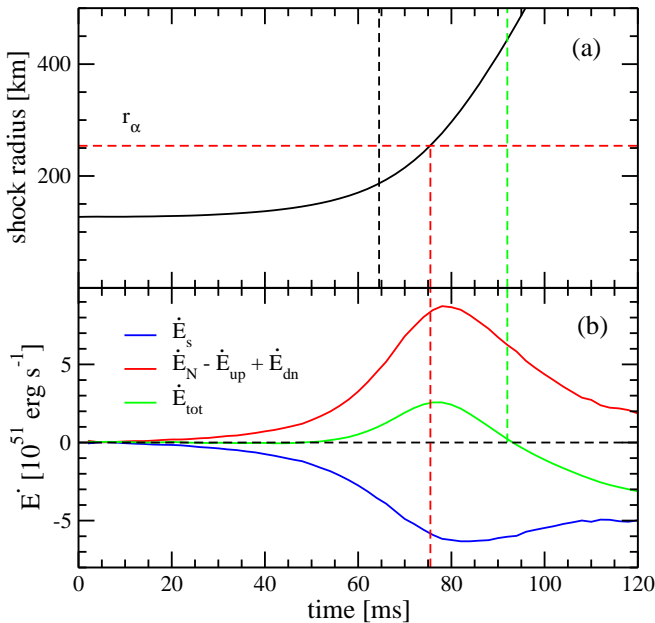


FIG. 7.— Same as Figure 5, but for a model that explodes via the non-oscillatory instability ( $L_{\nu_e, 52} = 4.6$ ). Only the two upper panels are shown, as the fluctuation in  $\dot{E}_{\text{up}}$  does not compensate  $\dot{E}_s$ , as in the last expansion of the oscillatory mode.

For oscillatory modes, we have found that instability sets in when the advection time through the gain region is longer than the time required to advect from the gain radius to a point close to the node in the density perturbation (Figure 6) times some coefficient close to unity. This is equivalent to requiring more mass to reside in the gain region than in the part of the cooling region above the node in the density perturbation, at any given instant (eq. [15]). To obtain a coefficient of unity, the relevant location is the radius at which the density and pressure perturbations are 180 degrees out of phase with each other. In the steady-state solution, and for most of our models, this position is approximately the radius closest to  $R_\nu$  where the specific cooling has decreased in magnitude by one e-folding from its maximum (e.g., Figure 1d).

The approximate instability criterion is then

$$t_{\text{adv-g}} > t_{\text{adv-e}}, \quad (24)$$

with

$$t_{\text{adv-g}} = \int_{R_g}^{R_s} \frac{dr}{|v_r|} \quad (25)$$

and

$$t_{\text{adv-e}} = \int_{r_e}^{R_g} \frac{dr}{|v_r|} \quad (26)$$

$$\left( \frac{\mathcal{L}_{\text{net}}}{\rho} \right) \Big|_{r_e} = \frac{1}{e} \left( \frac{\mathcal{L}_{\text{net}}}{\rho} \right) \Big|_{\text{min}}, \quad (27)$$

and where the solution to equation (27) closest to  $R_\nu$  is taken. The dependence of these two timescales on neutrino luminosity is shown in Figure 8.

It is worth emphasizing that  $r_e$  was chosen because it yields a coefficient of unity. Another location close to the node in the density perturbation could also have been used, with a slightly different coefficient. For example, taking the radius of maximum specific cooling  $r_{\text{cmax}}$  yields an instability condition  $t_{\text{adv,gain}} > 1.5t_{\text{cmax}}$ , where the latter timescale is computed

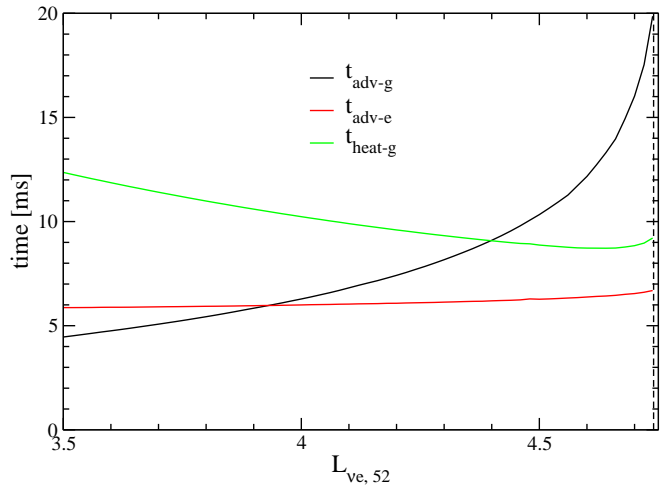


FIG. 8.— Characteristic timescales that determine the approximate instability condition for oscillatory and non-oscillatory modes, as a function of electron neutrino luminosity in our fiducial sequence (compare with Figure 4). Shown are the advection time over the gain region (black, eq. [25]), advection time from the gain radius to the point where cooling has decreased by an e-folding from its maximum (red, eq. [26]), and timescale to change the total energy in the gain region by neutrino heating (green, eq. [29]). The vertical dashed line marks the Burrows-Goshy limit.

by replacing  $r_e$  with  $r_{\text{cmax}}$  in equation (26).

A physical justification for  $r_e$  can be found by looking at the behavior of the relative phase between the pressure and density perturbations. It is a general result from stellar pulsation theory that, for oscillatory instability, an excitation mechanism is required which causes the system to be absorbing heat at the point of maximum compression (e.g., Cox 1974). This way, the pressure maximum is reached during the expansion phase, leading to positive work over an oscillation cycle, and hence to a net increase in the pulsation kinetic energy. In the system under study, such a phase lag of the pressure perturbation relative to the density is satisfied below the node of the density perturbation. The point where both perturbations are 180 degrees apart is approximately  $r_e$  for most of our models, with the pressure leading the density at any given radius above it<sup>7</sup>. In cases where  $r_e$  does not trace the phase radius correctly, the criterion in equation (24) loses accuracy. The relation between the phase radius and the cooling profile is most likely a consequence of the way we suppress the neutrino source terms with density (eq. [14]); different implementations of neutrino transport will most likely find slightly different values.

An interesting question is how the phase lag criterion for stars can be adapted to the problem at hand, given that fluid elements are advected downstream instead of returning to their original position. Taken at face value, the phase lag criterion would dictate that the driving region resides below the node of the density perturbation. However, the pressure lags the density in this region for both stable and unstable models, and  $r_e$  hardly changes over a wide range in  $L_{\nu_e}$  (Figure 8). Such question is likely to be at the root of the instability mechanism of long wavelength modes of the Standing Accretion Shock Instability (SASI, Blondin et al. 2003) with heating included, and will not be further pursued in this paper.

In the case of non-oscillatory modes, the instability threshold is very close to the point where the advection time through

<sup>7</sup> To determine the precedence of density or pressure maxima, we take two peaks that are closest in phase. This is only possible when perturbations have a phase shift different than 0 or 180 degrees.

the gain region is longer than the time required to change the total energy through heating,

$$t_{\text{adv-g}} > t_{\text{heat-g}} \quad (28)$$

with

$$t_{\text{heat-g}} = \frac{\int_{R_g}^{R_s} d^3x (\rho e_{\text{tot}})}{\int_{R_g}^{R_s} d^3x \mathcal{L}_{\text{net}}}. \quad (29)$$

The dependence of  $t_{\text{heat-g}}$  on neutrino luminosity is also shown in Figure 8. This relation has long been known to provide a predictive criterion for runaway expansion in spherically symmetric core-collapse simulations (Thompson et al. 2005; Buras et al. 2006a; Murphy & Burrows 2008; Marek & Janka 2009). Its interpretation is straightforward: neutrino heating is effective enough to change the internal energy of the flow during its transit time through the gain region. As a consequence, the pressure changes significantly and the shock readjusts to a new position (Janka & Keil 1998).

Note that equation (28) is a global condition on the gain region and includes the gravitational binding energy, differing from local definitions of this ratio such as those in Thompson et al. (2005) and Pejcha & Thompson (2011). The fluid does not achieve positive energy over a time  $t_{\text{adv-g}}$  ( $\sim 10$  ms, Figure 8), but instead takes a multiple of this timescale to transition into runaway expansion. As we discuss in the next section, onset of runaway occurs when the fluid achieves positive energy for the first time.

We have checked whether any instability threshold can be described by a fixed value of the parameter  $\chi$  that measures the effects of buoyancy in an advective flow,

$$\chi = \int_{R_g}^{R_s} |\omega_{\text{bv}}| \frac{dr}{|v_r|}, \quad (30)$$

where  $\omega_{\text{bv}}$  is the Brunt-Väisälä frequency,

$$\omega_{\text{bv}}^2 = \frac{GM}{r^2} \left( \frac{1}{\Gamma_s} \frac{\partial \ln p}{\partial r} - \frac{\partial \ln \rho}{\partial r} \right), \quad (31)$$

with  $\Gamma_s = (\rho/p)c_s^2$ . When  $\chi \gtrsim 3$ , buoyancy is expected to overcome the stabilizing effect of advection and lead to convective instability in the multidimensional case (Foglizzo et al. 2006). Even though all of our sequences have  $\chi$  in the range 1-10 near the threshold for instability, in none of them does this parameter have a constant value along the critical stability curves. For example, in our fiducial sequence, the value of this parameter at the non-oscillatory threshold ranges from  $\chi \simeq 7$  for  $\dot{M} = 0.1 M_\odot \text{ s}^{-1}$  to  $\chi = 1.7$  at  $\dot{M} = 1 M_\odot \text{ s}^{-1}$ . It is worth pointing out that the analysis of Foglizzo et al. (2006) applies to infinitesimal perturbations. The results of Scheck et al. (2008) show that the SASI can trigger convection through finite amplitude density fluctuations in cases where  $\chi < 3$ , so our findings do not necessarily imply that convection will be suppressed at large accretion rates in the quasi steady-state approximation (§2.1).

#### 4.4. Nonlinear Phase and Runaway Expansion

Once oscillatory modes become unstable, the amplitude grows steadily until the oscillation cycle is broken and the system transitions into runaway expansion. Figure 5 shows that not only the shock radius but also the different energy generation terms undergo a qualitative change in behavior relative to the linear phase once this point is reached. In particular, the

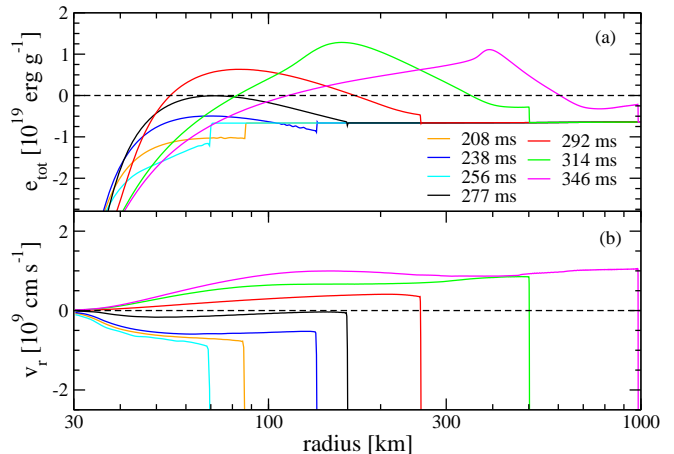


FIG. 9.— Total specific energy  $e_{\text{tot}}$  (a) and radial velocity (b) as a function of radius for the model shown in Figure 5, which explodes via the oscillatory instability. Different curves correspond to different times in the simulation, as labeled. The black curve (277 ms), red curve (292 ms), and green curve (314 ms) correspond to the vertical dashed lines of the same color in Figure 5a.

energy generation due to shock motion decouples from the fluctuation in the energy flux entering through the shock. Expansion is driven by the net energy generation from accretion, with damping from the shock motion term.

A physical origin for this transition point can be found by inspecting the evolution of the total specific energy and radial velocity in the system. Figure 9 shows that this time corresponds approximately to the point where the specific energy behind the shock becomes positive for the first time. This time is marked by a vertical black dashed line in Figure 5a and the snapshot at 277 ms in Figure 9. At about the same time, the fluid just inside the shock achieves positive radial velocity, reversing the accretion flow. This transition point is equivalent to the *escape temperature* condition discussed in Burrows et al. (1995).

Physically, the above result is dependent on the definition of the zero points of energy in the context of a Newtonian framework. The EOS used here takes this zero point to be, per baryon, the atomic mass unit (Shen et al. 1998). Our expression for the total specific energy, equation (17), takes the zero point of gravitational binding energy at an infinite distance from the central mass. Given these definitions, the condition of positive energy leading to runaway expansion is a well-defined mathematical concept. A self-consistent determination of this condition would require inclusion of the rest mass energy and gravitational field calculated self-consistently in a general relativistic framework.

The shock accelerates when it approaches the radius where the binding energy of alpha particles equals their gravitational binding energy (eq. [11]). This can be understood from the fact that the dissipation due to shock motion  $\dot{E}_s$  decreases in magnitude with increasing radius, because the total specific energy behind the shock becomes less negative. This can be seen in Figure 5b, where the blue curve reaches a minimum value. By now most of the gain region has reached positive energy, except for a narrow layer behind the shock, and most of the fluid has positive velocity, effectively becoming a wind-like solution.

A final transition occurs when the shock begins to mechanically decouple from the protoneutron star atmosphere. This occurs approximately at a time when the sound crossing time from the shock to  $R_\nu$  becomes longer than the shock expansion time  $R_s/v_s$ , where  $v_s$  is the shock velocity. This time is

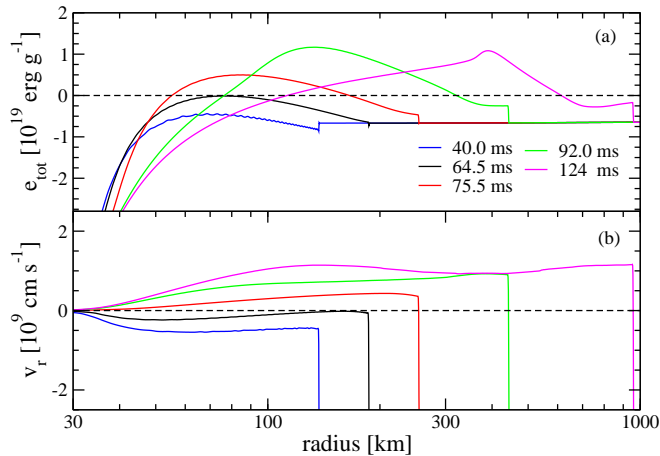


FIG. 10.— Same as Figure 9, but for the model shown in Figure 7, which explodes via the non-oscillatory instability. Black (64.5 ms), red (75 ms), and green (92 ms) curves correspond to the times signaled by vertical dashed curves of the same color in Figure 7.

marked as a vertical green dashed line in Figure 5a and corresponds to the curve at 314 ms in Figure 9. This mechanical decoupling explains the fact that the net energy generation becomes negative yet the shock continues to expand, as inferred from Figure 5. It is worth noting that velocities below the shock are subsonic throughout the time period considered here.

Non-oscillatory modes transition directly into runaway expansion, and their evolution closely resembles that of oscillatory modes after reaching positive energy. The corresponding snapshots of total specific energy and radial velocity at different phases are shown in Figure 10.

In all of the sequences simulated, transition to runaway expansion is achieved after the flow becomes radially unstable. We have found no unstable mode that saturates, nor any model that having achieved positive energy, failed to continue into runaway expansion. Our preliminary conclusion is that for the set of assumptions adopted in this paper, radial instability is a sufficient condition for transitioning into runaway expansion.

#### 4.5. Conditions for Saturation

There are many examples in the literature where one-dimensional stalled shocks start to expand or oscillate, but then fizzle (e.g., Figure 1 of Janka & Müller 1996). It is thus imperative to identify the processes that can lead to saturation, as our preliminary finding linking instability to runaway may break down in some region of parameter space.

Insight on this question can be obtained again by inspecting the different processes that contribute to the change in the total energy in the post-shock region (eq. [19]). What we are interested in are dissipation processes that contribute with negative energy generation.

In the present study, we are ignoring evolution of the neutrinospheric parameters ( $R_\nu$ , core luminosities, and spectra) and heating due to the accretion luminosity, hence the dominant dissipation mechanism arises from the change in the post-shock volume,  $\dot{E}_s$ , as inferred from Figures 5 and 7. This term is made up of three factors: (1) the specific energy below the shock, (2) the density profile, and (3) the rate of change of the post-shock volume.

1. At the typical radii where supernova shocks stall (100–200 km), the total specific energy  $e_{\text{tot}}$  is usually nega-

tive. Because the temperature decreases outward, nucleons below the shock recombine first into alpha particles and then heavy nuclei as the shock moves out, yielding an increase in the thermal energy that is comparable to the gravitational binding energy (Bethe 1996; Fernández & Thompson 2009a). This causes the total specific energy to become significantly less negative, decreasing the size of  $\dot{E}_s$  as the shock expands. This can be most clearly seen in Figure 5b, which shows a clear transition in the evolution of  $\dot{E}_s$  when the shock reaches  $r_\alpha$ . The results of Fernández & Thompson (2009a) show that using a constant dissociation energy indeed quenches runaway expansion, in direct contrast to allowing alpha particles to recombine, because in the first case the dissociation energy becomes an increasingly larger fraction of the local gravitational binding energy as the shock expands. Even then, saturation occurs at a radius that is several times the initial shock radius. Except for unrealistically small shock stagnation radii ( $\lesssim 50$  km), this saturation channel is unlikely to be of importance.

2. The evolution of the density profile below the shock and the mass accretion rate are tied to the density profile of the progenitor at the onset of collapse. For an iron core supported by relativistic electrons the density scales like  $r^{-3}$ , yielding a mass accretion rate that scales inversely with time at a fixed radius when mass conservation and a near free-fall velocity field are assumed (Bethe 1990). A time-independent mass accretion rate corresponds to a progenitor density profile  $\propto r^{-3/2}$ , which would be given by an adiabatic index of 5/3 in hydrostatic equilibrium. In other words, a time-independent mass accretion rate, as assumed in our sequences, is already unrealistically high and overestimates the dissipation.
3. Because  $\dot{E}_s$  is negative on expansion, it tends to stabilize the shock velocity for a given energy dissipation rate. The dominant energy source for expansion is neutrino heating. As long as the total heating remains larger than  $\dot{E}_s$  before the shock is completely decoupled from the atmosphere, the shock will continue to expand.

We therefore conclude that for the physical assumptions of the present study, *radial instability is a sufficient condition for runaway expansion*.

In the general case, however, evolution of the neutrinospheric parameters and neutrino heating by the accretion luminosity can provide significant energy dissipation and saturate the instability. By inspection of equation (18), one can find three sources of negative energy.

First, evolution of the core neutrino flux affects the energetics via  $\dot{E}_N$ . If the net effect of decreasing neutrino luminosities and increasing mean neutrino energies is a decrease in the energy deposition in the gain region, the instability can be suppressed in two ways. The linear instability depends on the extent of the gain region through  $t_{\text{adv, gain}}$ , hence a rapid decrease of heating can stabilize oscillations or non-oscillatory expansion if the flow has not yet achieved positive energy when the stability criterion is reversed. Second, a decrease in the rate of neutrino energy deposition can lead to quenching of the runaway phase if the total rate of heating fails to keep up with

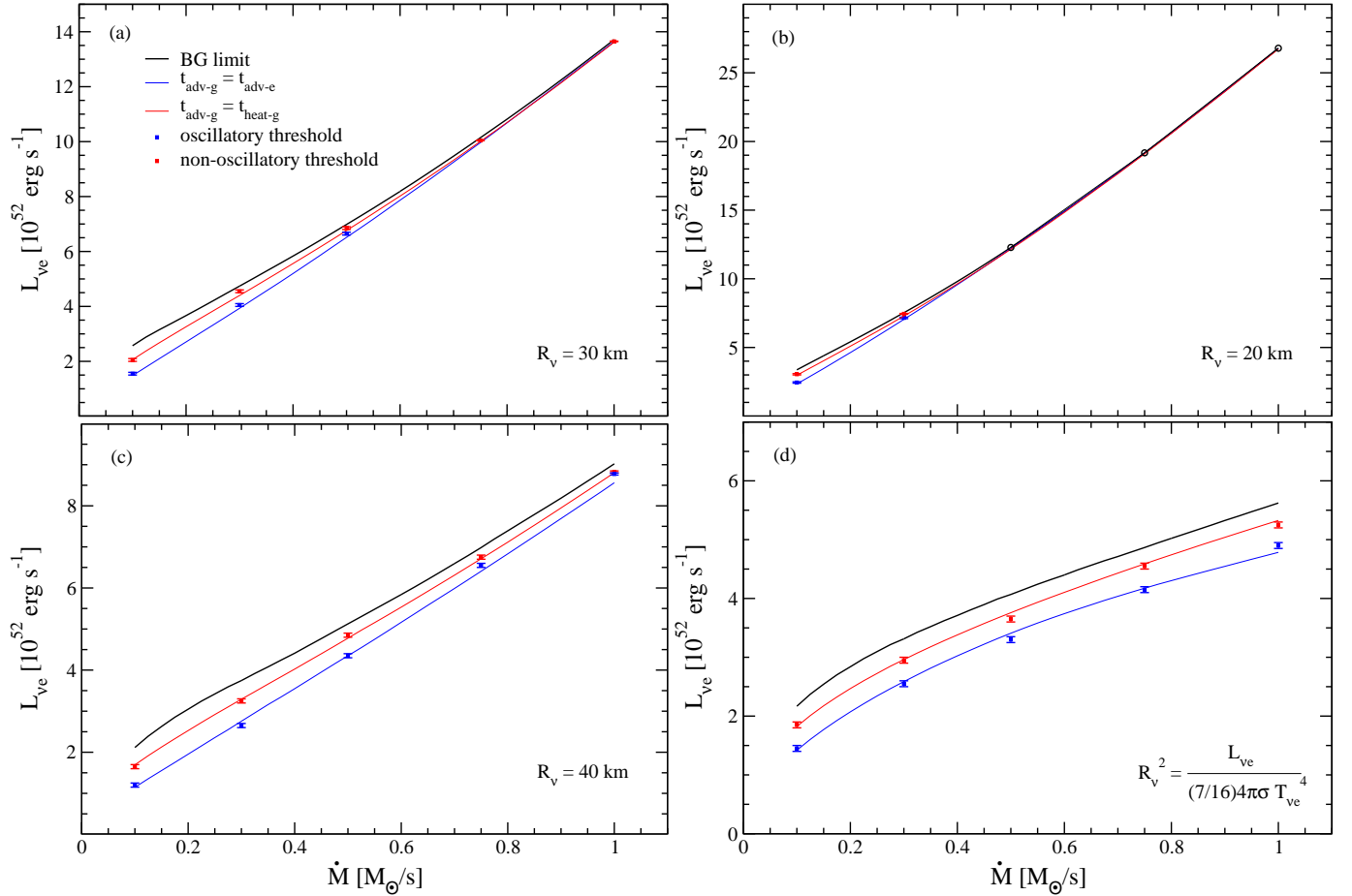


FIG. 11.— Threshold electron neutrino luminosity for radial instability as a function of mass accretion rate, for different sequences of models. Panels (a), (b), and (c) correspond to sequences with fixed neutrinospheric radii at  $R_\nu = \{30, 20, 40\}$  km, respectively, while the sequence in panel (d) relates  $R_\nu$  to the neutrino luminosity via the black body relation (§2.5). Data points denote results from time-dependent simulations, where the threshold for explosion is taken as the average between stable and unstable models, with the error bars showing the size of the difference in  $L_{\nu_e}$  ( $\Delta L_{\nu_e} < 10^{51}$  erg s $^{-1}$ ). Blue points correspond to oscillatory and red to non-oscillatory instability, respectively. Curves correspond to our approximate instability criteria for oscillatory (blue, eq. [24]), and non-oscillatory modes (red, eq. [28]). Black curves correspond to the limiting luminosity of the steady-state configuration at constant optical depth, calculated as described in §3. Black circles in panel (b) denote the absence of instability (and thus explosion) for  $\dot{M} \geq 0.5 M_\odot$  s $^{-1}$  for all luminosities up to and including the Burrows-Goshy limit.

dissipation due to  $\dot{E}_s$ . The results of Janka & Müller (1996) are consistent with the operation of this saturation channel.

Second, the contribution of the accretion luminosity to the total neutrino flux in realistic models is  $\sim 50\%$  (e.g., Liebendörfer et al. 2001). The important aspect to keep in mind here is that shock expansion relative to its steady-state position leads to a decrease in the magnitude of the mass accretion rate. Perturbing the mass conservation equation yields (Foglizzo et al. 2007)

$$\frac{\delta \dot{M}}{\dot{M}} = \left( \frac{1}{v_2} - \frac{1}{v_1} \right) \delta v_s, \quad (32)$$

where  $v_1$  and  $v_2$  are the (negative) upstream and downstream fluid velocities, and  $\delta v_s$  is the shock velocity perturbation. Taking  $\delta v_s$  real and positive (shock expansion) yields  $\delta \dot{M}/\dot{M} < 0$ , or a decrease in the magnitude of the accretion rate. Hence including the heating from accretion neutrinos adds a non-trivial feedback to both oscillatory and non-oscillatory modes, altering the instability criteria. Buras et al. (2006b) find that indeed spherical oscillations are damped by the decrease in the heating due to the dropping mass accretion rate. As noted by a number of previous works, the runaway expansion phase also cuts off accretion in spherical symme-

try. A larger core neutrino flux is therefore required to sustain expansion, relative to the light bulb heating case, and the causality relation between radial instability and explosion we have found here will be violated.

Finally, the contraction of the protoneutron star generates in itself a sink of energy in the post-shock region. Including this effect, and keeping everything else constant, would add a term of the form

$$\dot{E}_{\nu\text{sph}} = -4\pi R_\nu^2 \dot{R}_\nu (\rho e_{\text{tot}})_{R_\nu} \quad (33)$$

$$\simeq -10^{50} R_{\nu,30}^2 \dot{R}_{\nu,6} \rho_{11} e_{\text{tot},19} \text{ erg s}^{-1} \quad (34)$$

to equation (18), with  $R_{\text{in}} = R_\nu$ . The notation in the second equality is  $R_{\nu,30} = R_\nu/(30 \text{ km})$ ,  $\dot{R}_{\nu,6} = \dot{R}_\nu/(-10^6 \text{ cm s}^{-1})$ ,  $\rho_{11} = \rho/(10^{11} \text{ g cm}^{-3})$ , and  $e_{\text{tot},19} = e_{\text{tot}}/(-10^{19} \text{ erg g}^{-1})$ . In contrast to  $\dot{E}_s$ , contraction leads to energy dissipation. This quantity is smaller than typical core neutrino luminosities, but approaches the net energy generation terms that regulate instabilities (§4.2). A more careful analysis would need to include the additional cooling and heating by accretion neutrinos generated by enlarging the post-shock cavity. The one-dimensional results of Janka & Müller (1996) show that indeed  $\sim 10\%$  higher core neutrino luminosities are required to

start an explosion in models that experience protoneutron star contraction relative to fixed cores, when all other parameters are similar.

## 5. INSTABILITY THRESHOLDS AND RELATION TO THE LIMITING STEADY-STATE LUMINOSITY

### 5.1. Dependence on Mass Accretion Rate and Neutrinospheric Radius

For each of the simulation sequences described in §2.5, we have searched for the instability thresholds of oscillatory and non-oscillatory modes. Figure 11 shows the resulting threshold luminosities as a function of mass accretion rate. In all cases, data points correspond to the average luminosity between two models at both sides of the instability threshold. The separation in luminosity, shown as error bars, is less than  $10^{51}$  erg  $s^{-1}$ .

Figure 11 also shows the limiting luminosity for a steady-state configuration (the Burrows-Goshy limit), calculated as described in §3. The resulting curve agrees qualitatively with the results of Burrows & Goshy (1993), Yamasaki & Yamada (2005, 2006), and Pejcha & Thompson (2011). Note that the neutrinospheric temperatures, neutrino opacities, and EOS employed here differ from what was used in those studies, hence numerical values are expected to differ.

The calculation of this limiting luminosity in a consistent manner with the microphysics, initial conditions, and boundary conditions employed in our simulations allows direct testing of the hypothesis that the critical stability threshold for explosion is given by the Burrows-Goshy limit. We find that in all cases, the measured thresholds for both type of mode lie below this limiting value. When the neutrinospheric radius is held constant, the instability thresholds approach (but never equal) the Burrows-Goshy limit for increasing mass accretion rate. In the sequence that relates the neutrinospheric radius to the neutrino luminosity via the black body relation (Figure 11d), the instability thresholds have a nearly constant separation in luminosity over the entire range of accretion rates investigated.

The sequence with  $R_\nu = 20$  km yielded unexpected results for  $\dot{M} \geq 0.5M_\odot s^{-1}$ , however. In this case there is neither instability nor runaway for all luminosities up to and including the limiting value, independent of numerical resolution. Our approximate instability criteria fail to predict this behavior, showing that additional constraints play a role in determining instability. Also, the fact that no explosion is found at the Burrows-Goshy limit shows that this luminosity is not an independent tracer of stability either. Increasing the neutrino luminosity above the limiting value (at constant shock radius) by  $\sim 10\%$  causes the shock to readjust to a new equilibrium position, which is also stable. It is worth noting however that the shock radius is  $R_s \leq 61$  km for the non-exploding segment of this sequence. This is an unrealistically low value, with advection times of the order of  $\sim 3$  ms, a factor of a few from the dynamical time. It is likely that the fixed value of  $r_{vf}$  used to set the upstream velocity (§2.3) leads to these extreme conditions.

In all other sequences, the approximate instability criteria found in §4.3 provide a good description of the measured values over a wide region of parameter space, with agreement better than 5% in  $L_{\nu_e}$ . They correctly capture the disappearance of the oscillatory mode in the  $R_\nu = 30$  km sequence at high accretion rates, where only a non-oscillatory mode is measured. This phenomenon occurs because at large accre-

tion rates, the shock radius becomes increasingly smaller. The size of the resulting gain region is such that the advection time through it never exceeds  $t_{adv-g}$  before the heating time drops below  $t_{adv-g}$  due to the increasing luminosity. The deviation of the measured oscillatory threshold from the approximate criterion at high accretion rate in the  $R_\nu = 40$  km sequence is due to  $r_e$  not being a good tracer of the point where pressure and density perturbations are 180 degrees out-of-phase (§4.3).

Our results extend the findings of Yamasaki & Yamada (2007), who obtained  $\ell = 0$  instability thresholds below the Burrows-Goshy limit, to a wider region of parameter space. Our results are quantitatively different from theirs, partly due to the different neutrinospheric temperatures that they employed ( $T_{\nu_e} = T_{\bar{\nu}_e} = 4.5$  MeV), their use of the pure absorption coefficient for computation of the optical depth (see §2.3 and §5.2), and their inclusion of self-gravity. Using the same parameters as Yamasaki & Yamada (2007), we obtain a limiting luminosity of  $L_{BG,\nu_e} = 7.36 \times 10^{52}$  erg  $s^{-1}$  for  $\dot{M} = 1M_\odot s^{-1}$ , which differs by a factor of nearly two, and is closer to what was found originally by Burrows & Goshy (1993). The corresponding approximate instability criteria for oscillatory and non-oscillatory modes are  $6.41 \times 10^{52}$  erg  $s^{-1}$  and  $7.04 \times 10^{52}$  erg  $s^{-1}$ . These values are lower than our limiting luminosity by 13% and 5%, respectively.

### 5.2. Other Parameter Dependencies

Given the parametric character of this study, certain choices had to be made in order to construct a background flow that is as realistic as possible. Here we explore how our results depend on numerical resolution, boundary conditions, parameters that determine the upstream flow, and the suppression of source terms near the neutrinosphere.

Figure 12a shows the approximate instability criteria and Burrows-Goshy limit for our fiducial sequence, together with instability thresholds measured from simulations at different resolutions. The grid is chosen logarithmically spaced, with a ratio of spacing between adjacent cells  $\zeta = (R_{max}/R_\nu)^{1/N_r}$ , and  $\Delta r_{min} = R_\nu(\zeta - 1)$ , with  $\Delta r_{min}$  the cell adjacent to the inner boundary (Appendix B). Oscillatory modes asymptote to the theoretical threshold for increasing resolution, albeit convergence is non-monotonic. Non-oscillatory modes converge monotonically to a slightly different value, indicating that the instability criterion is indeed approximate.

The results shown in Figure 12 also indicate that previous hydrodynamic studies that used similar methods to solve the hydrodynamic equations (Murphy & Burrows 2008; Nordhaus et al. 2010; Hanke et al. 2011) have enough resolution to capture the critical stability thresholds correctly. However, we have found in our models that there are noticeable differences in the growth rates of oscillatory modes as a function of resolution. For the model with  $L_{\nu_e,52} = 4.1$  in our fiducial sequence, the time delay to explosion varies by  $\sim 100$  ms when going from  $N_r = 240$  to  $N_r = 3200$ . True convergence, in the sense that the fractional deviations in the shock radius evolution are much less than unity for models at different resolutions, is only achieved for  $N_r \geq 1600$  with our fiducial parameters. It is not straightforward to prescribe a definite resolution required for convergence given a hydrodynamic method, however, as the implementation of the microphysics (tabular in our case) also influences this number. A set of standard hydrodynamic tests tailored specifically for the supernova problem would be helpful in assessing the reliability of results associated with a given implementation.

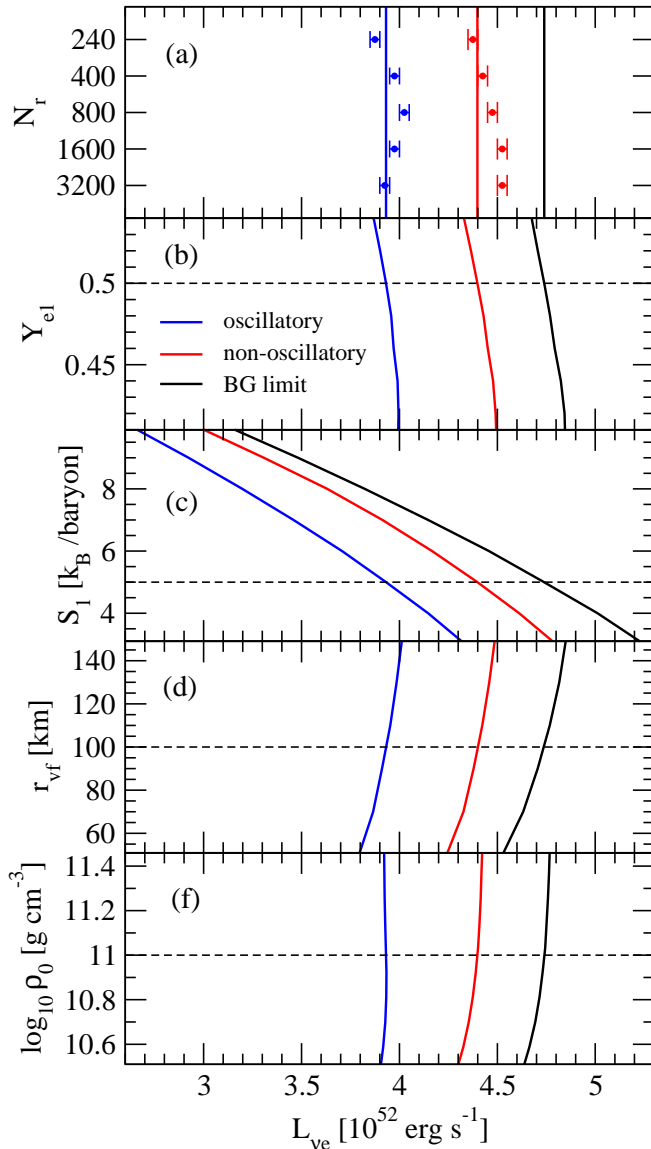


FIG. 12.— Dependence of the approximate instability thresholds and Burrows-Goshy limit on various parameters, taking our fiducial sequence as baseline. Solid lines denote the approximate instability condition for oscillatory (blue, eq. [24]) and non-oscillatory modes (red, eq. [28]), respectively, while the black solid line denotes the Burrows-Goshy limit. Panel (a) shows simulation results (as data points) as a function of radial resolution in a logarithmic grid from 30 km to 1000 km. Other panels show the dependence of these critical points on the upstream electron fraction (b), upstream entropy (c), radius at which upstream velocity is set to the free-fall speed (d), and density cutoff for source terms (e, eq. [14]). Parameters of our fiducial sequence are denoted by a black dashed line.

To test the influence of the steady-state boundary condition on our results, we have evolved a sequence with a different inner boundary condition, which allows an arbitrary amount of mass to leave the domain, while providing enough pressure support to prevent the shocked envelope from collapsing (§2.4). Figure 13a shows that the system still goes through the same stability phases as the neutrino luminosity is increased, with a small quantitative difference  $\lesssim 5\%$  in the critical stability points relative to our fiducial sequence. We thus conclude that the two types of instability do not depend on the fluxes of mass, momentum, and energy leaving the domain being fixed. The quantitative differences can be explained by the fact that the outflow boundary condition acts as a persistent source of

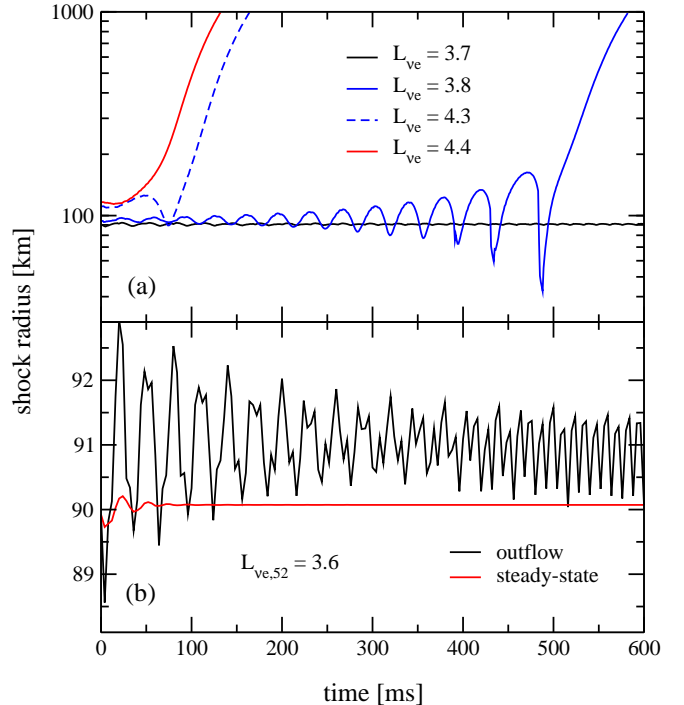


FIG. 13.— Evolution of the shock radius in selected models of our fiducial sequence using different prescriptions for the inner boundary condition. Panel (a) shows models with different neutrino luminosities using the outflow boundary condition (eqns. [12]-[13]). The curves shown bracket the instability threshold for oscillatory (black and solid blue) and non-oscillatory (dashed blue and red) modes. Except for the boundary condition, parameters are identical to those in Figure 4. Panel (b) compares two runs with the same parameters except the inner boundary condition. Both models are stable and do not explode (note the vertical scale).

waves, keeping shock oscillations at some non-zero amplitude. This effect is shown in Figure 13b, which compares the shock radius evolution for two stable runs with identical parameters except for the boundary condition.

This small quantitative difference, caused by a persistent wave source, is interesting as it provides an illustration of what we expect will occur in the multidimensional case. The critical stability thresholds are modified in the presence of this additional wave generation, as comparison of Figures 4 and 13 show. Taking the time-average of two stable runs with differing boundary conditions after they have settled into steady- or quasi-steady-state, shows that the mean velocity profiles differ (Figure 14). The magnitude of the change in the threshold luminosities is consistent with the magnitude and direction of the changes in the approximate instability criteria, using the mean advection times rather than the unperturbed ones. A stronger source of wave energy (e.g., convection) will affect the mean advection time in stronger way, and critical stability points will move accordingly.

Figures 12b-e illustrate the sensitivity of the approximate instability thresholds and the Burrows-Goshy limit to the parameter choices made in §2.3. Shown is the dependence on the upstream electron fraction, upstream entropy, radius at which the upstream flow has free-fall speed, and cutoff density for neutrino source terms (eq. [14]). There is a somewhat sensitive dependence on the upstream entropy, which in a realistic situations will be set by the entropy in the progenitor core. Note that larger luminosities are needed to cause stalled shocks to become unstable when the progenitor entropy is smaller. Nonetheless, the relation between the approximate

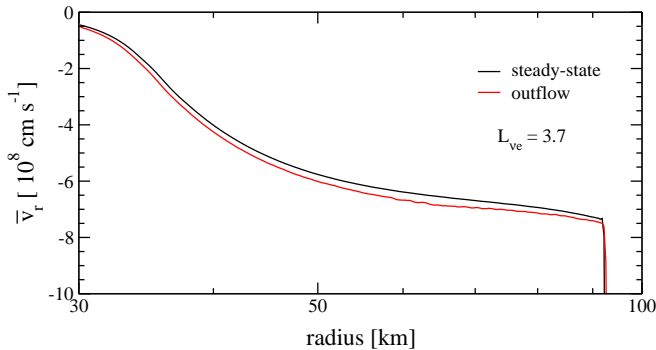


FIG. 14.— Time averaged radial velocity as a function of radius for two stable models in our fiducial sequence with the same parameters except the inner boundary condition. The time average is taken after the models have settled into a steady- or quasi-steady state.

thresholds and the Burrows-Goshy limit persists without qualitative changes. All other parameters produce changes smaller than  $\sim 5\%$  over a large range of values.

We have also examined the robustness of the hierarchy between instability thresholds and Burrows-Goshy limit when the quantities used to calculate the latter are changed. Figure 15a shows the effect of increasing or decreasing the neutrinospheric optical depth (eq. [8]) by a factor of two. Neither of these changes cause the Burrows-Goshy limit or instability thresholds to cross each other, for a given optical depth. This result can also be seen from the non-overlapping curves in Figure 2 for fixed accretion rate. Interestingly, the exact optical depth chosen seems to matter the least when going to low mass accretion rates.

The dependence on the choice of neutrino opacity is shown in Figure 15b. Here we compare the effects of using the pure absorption, effective, or total (absorption plus scattering) opacity (§2.3) in equation (8). Again, the three curves maintain their relative hierarchy and do not cross for a given choice of opacity.

### 5.3. Relation between the Burrows-Goshy Limit and the Instability Thresholds

We have found that the difference between the Burrows-Goshy limit and the radial instability thresholds is finite and measurable, and is independent of parameter choices. However, the question remains as of why is this limiting luminosity always close to the threshold for non-oscillatory instability in the parameter region relevant to core-collapse supernovae.

In a more extended parameter space study of steady-state configurations, Pejcha & Thompson (2011) found that at the Burrows-Goshy limit, the ratio between  $t_{\text{adv-g}}$  and the global heating timescale (without gravity) is always close to unity. Ultimately, this proximity must depend on the characteristic magnitude of the neutrino opacities, the gravitational binding energy around a forming neutron star, and the fact that the flow is supported against gravity by the thermodynamic pressure of the gas (e.g., not centrifugal forces). In other words, it could be just a result of dimensionality. A possible way to test this hypothesis is to explore the behavior of the system at lower mass accretion rates, where the expected trend is an increasing deviation.

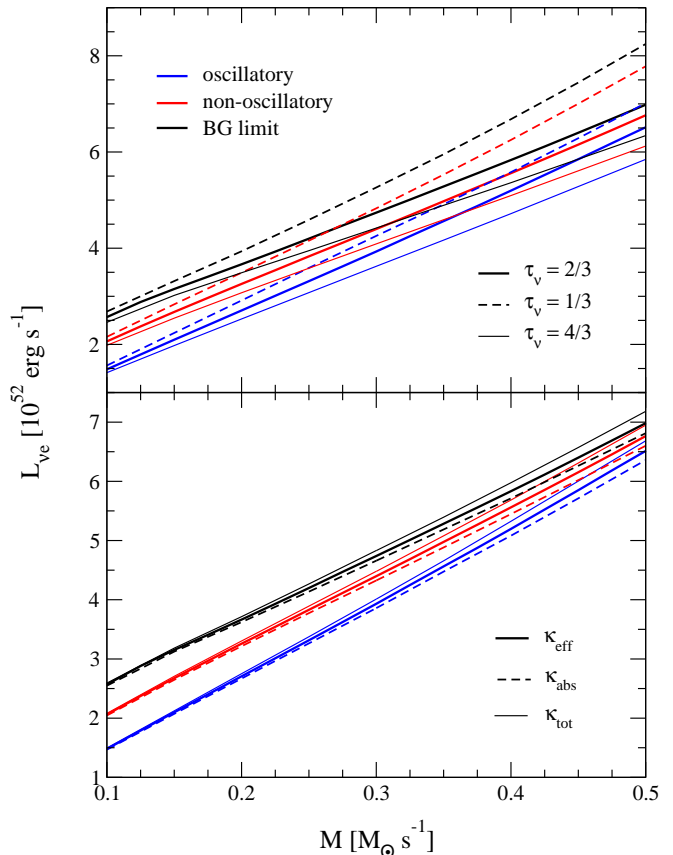


FIG. 15.— Approximate instability thresholds and Burrows-Goshy limit as a function of mass accretion rate for different optical depths (top) and different prescriptions for the neutrino opacity (bottom). The three curves remain separated.

## 6. SUMMARY AND DISCUSSION

We have investigated the transition to runaway expansion of a stalled core-collapse supernova shock in spherical symmetry, when the parameters that describe the accretion flow are varied systematically. A realistic equation of state and weak interactions were employed to perform time-dependent simulations with FLASH3.2. Starting from steady-state solutions to the hydrodynamic equations, we evolve sequences of time-dependent models with increasing neutrino luminosity, and analyze the hydrodynamic processes that mediate the transition from accretion to runaway expansion. Our findings can be summarized as follows:

1. – The onset of radial instability is a sufficient condition for runaway expansion when heating by the accretion luminosity is ignored and neutrinospheric parameters remain constant in time. Radial instability can manifest itself via oscillatory and non-oscillatory modes, as found in the linear stability analysis of Yamasaki & Yamada (2007) and numerous time-dependent hydrodynamic studies. These modes are non-adiabatic, as they involve changes in the heat content of the fluid (§4.2).
2. – For both types of modes, transition to runaway expansion occurs after a portion of the fluid in the gain region achieves positive energy. This coincides with the fluid just below the shock achieving positive velocity, starting the phase of runaway expansion (§4.4; Figures 9 and 10).

3. – The only significant source of dissipation in our models is the energy loss from shock motion (eq. [23]; Figures 5 and 7), which provides damping on expansion. Nuclear recombination and a steady source of neutrino heating combine to ensure that this term never extinguishes the runaway or saturate the linear instability. In a more realistic context, the dominant dissipative processes are the decrease of the core neutrino luminosity with time, and self consistent heating by the accretion luminosity. The latter is expected to provide a negative feedback during expansion due to the decrease of the mass accretion rate (e.g., Janka & Müller 1996). The contraction of the protoneutron star is a somewhat smaller correction, of the order of  $\sim 10\%$ . None of these effects is included in this study (§4.5).

4. – We have found approximate instability criteria for oscillatory and non-oscillatory modes that correctly describe the behavior of the system over a wide region of parameter space, with a precision better than 5% in neutrino luminosity (§4.3; Figure 11). For oscillatory modes, instability arises when the advection time over the gain region becomes longer than the advection time from the gain radius to the point where the pressure and density perturbations are 180 degrees out of phase (Figures 6 and 8). In our implementation, this point lies at a position in the background flow where the cooling has decreased by an e-folding from its peak value. This equality of advection times is equivalent to an equality of masses of the respective regions when the accretion rate is constant. We have not been able to identify a conclusive physical reason for why this condition on the masses or advection times triggers an oscillatory instability. We surmise that a relation might exist between the fraction of the oscillation cycle that the fluid gains energy and the phase lag criterion in stellar pulsation theory (e.g., Cox 1974).

4. – Non-oscillatory modes become unstable when the advection time through the gain region becomes longer than the integrated total energy divided by the integrated net heating in the gain region. This condition means that heating is effective at increasing the thermal energy while the fluid transits the gain region, increasing the pressure and causing the shock to adjust to a new equilibrium position (Janka & Keil 1998). This global criterion has been used by a number of previous studies as an explosion diagnostic (Buras et al. 2006a; Murphy & Burrows 2008; Marek & Janka 2009).

5. – The instability thresholds are in general different from the limiting luminosity for the steady-state system (Burrows & Goshy 1993, §3). For constant neutrinospheric radius and increasing accretion rates, the thresholds asymptote to the limiting luminosity, but never coincide with it (Figure 11). This separation does not depend on how this limiting luminosity is calculated (Figure 15), or on specific parameter choices (Figure 12).

6. – The existence of a limiting luminosity for steady-state solutions is a direct consequence of requiring the optical depth between the neutrinosphere and the shock to have a fixed value (Figure 2). For fixed upstream conditions and increasing neutrino luminosity, the entropy increases and hence the radius at which the pressure transitions from being dominated by relativistic particles to being dominated by non-relativistic nucleons moves inward (Figure 3). This causes the density profile to soften at fixed radius, resulting

in a lower density at the neutrinosphere. Above a certain limit, there is not enough mass to provide sufficient neutrino optical depth to satisfy the closure relation, and no steady-state solution is possible. This result is equivalent to that of Pejcha & Thompson (2011), differing only in which boundary conditions are assumed to be fulfilled.

7. – We find neither instability nor explosion in our sequence with constant  $R_\nu = 20$  km for  $\dot{M} \geq 0.5M_\odot \text{ s}^{-1}$  and luminosities up to and including the limit luminosity (Figure 11b). At the lower end of these mass accretion rates, the shock radius is  $R_s \simeq 60$  km, and decreases for larger accretion rates. We did not find an explanation for this result within our framework. Regardless of the reason, however, it shows that the transition to runaway expansion does not necessarily occur at the limiting luminosity. It also shows that the approximate instability criteria derived here are incomplete, as an additional constraint is likely to determine the stability of the flow.

Our results show that the Burrows & Goshy (1993) conjecture, relating the transition to explosion to a global instability of the shocked envelope, is correct within a restricted set of assumptions. The critical stability surface, however, is not given by the limiting luminosity of the steady-state configuration. This limiting luminosity remains nonetheless close to the instability threshold over a large section of the parameter space relevant to core-collapse supernovae, a result that we have not accounted for and which deserves further investigation.

Murphy & Burrows (2008) and Fernández & Thompson (2009a) have also found oscillations around the transition to explosion. However, the width in neutrino luminosity separating exploding from non-exploding configurations is larger in those studies. In the case of Fernández & Thompson (2009a), this can be attributed to the differences in the employed microphysics relative to the present study. Large amplitude oscillations are excited in the simulations of Murphy & Burrows (2008) when the Si/O composition interface is accreted through the shock. Stable models damp oscillations, and unstable modes explode, with neutrally stable oscillations confined to a range  $\Delta L_{\nu_e}/L_{\nu_e} \simeq 4\%$ . This range is wider than that found here, presumably because Murphy & Burrows (2008) include the contraction of the protoneutron star. Our results are in good agreement with those of Ohnishi et al. (2006), who used essentially the same physical assumptions as we do.

The main result of this paper, point (1) above, does not apply to all modes of higher dimensionality. Non-radial oscillatory instability of the shock (the SASI) does not necessarily lead to explosion when the same set of assumptions adopted in this study are employed (Ohnishi et al. 2006). Given our results and those of Yamasaki & Yamada (2007), the question then arises as to whether a multi-dimensional explosion can be thought of as the excitation of an unstable radial-oscillatory, and/or non-oscillatory mode (radial or otherwise) by the action of turbulent stresses from the SASI and convection. In this case, the excited mode would arise from a background state that differs from the laminar steady-state solution by the presence of a turbulent pressure term in the momentum equation and a convective flux term in the energy equation. The excited mode would also become unstable at a lower neutrino luminosity than in the spherically symmetric flow.

According to Yamasaki & Yamada (2007), the non-radial-non-oscillatory modes that have the lowest threshold luminosities

ity for instability have Legendre indices  $\ell \sim 6$ . These modes are likely to be associated with convection in the gain region, as they have no unstable oscillatory counterpart. The results of Ohnishi et al. (2006) and Iwakami et al. (2008) show that small-scale convection in itself does not lead to runaway expansion. In contrast, an  $\ell = 1$  or  $\ell = 2$  non-oscillatory mode, such as that envisioned by Thompson (2000), is likely to be behind unipolar or bipolar explosions seen in axisymmetric simulations (e.g., Scheck et al. 2006). The results of Yamasaki & Yamada (2007) show that the threshold luminosities of these large scale non-oscillatory modes are larger than that of  $\ell \geq 3$  modes, and very close to that of the spherical oscillatory mode.

Which of these modes is excited first in a multidimensional context will obviously depend on the nature of the new background flow. The exploding three-dimensional models of Nordhaus et al. (2010) and Hanke et al. (2011) lack a dominant oscillatory mode in their transition to explosion, even though oscillations in the average shock position are still visible (particularly for the  $L_{\nu_e} = 9 \times 10^{51} \text{ erg s}^{-1}$  model in the  $11.2M_{\odot}$  progenitor sequence of Hanke et al. 2011). In contrast, two-dimensional models have a noticeable radial oscillatory component, with successive dips in the average shock radius before and during runaway expansion. Yet the amplitude of these oscillations is smaller than in the spherically symmetric case, suggesting that more than one mode is likely to be involved.

Support for this interpretation of multidimensional explosions can be found in the results of Buras et al. (2006a) and Marek & Janka (2009), who use the same definition of  $t_{\text{heat-g}}$  as we do here. They find that the ratio  $t_{\text{adv-g}}/t_{\text{heat-g}}$  exceeding unity corresponds roughly to the time when the shock begins its expansion towards explosion in two-dimensional runs. Obviously all the saturation mechanisms discussed in §4.5 are present in those simulations, so analogies need to be made cautiously. A similar result is obtained by Murphy & Burrows (2008), with a heating time defined without gravity and ki-

netic energy.

An attempt to include the effects of convection in the steady-state solution was made by Yamasaki & Yamada (2006), setting the convective flux to a value that yielded a flat entropy gradient. With this maximally efficient convection, they found that the Burrows-Goshy limit can decrease by several tens of percent relative to the laminar case. This would entail a corresponding decrease in the approximate instability thresholds found in this paper. A more careful treatment of the turbulent transport terms, along the lines of Murphy & Meakin (2011), could be used to construct quasi-steady-state flows and to perform a linear analysis like that of Yamasaki & Yamada (2007), helping to elucidate these questions with semianalytic tools.

The extension of our model to two- and three spatial dimensions will be discussed in a companion paper.

I thank Aristotle Socrates, Thomas Janka, Thierry Foglizzo, Jeremiah Murphy, Adam Burrows, Jason Nordhaus, and Boaz Katz for stimulating discussions. I also thank Evan O'Connor for help with the EOS implementation. Comments on the manuscript by an anonymous referee provided useful feedback and helped to improve the presentation. The author is supported by NASA through Einstein Postdoctoral Fellowship grant number PF-00062, awarded by the Chandra X-ray Center, which is operated by the Smithsonian Astrophysical Observatory for NASA under contract NAS8-03060. This research was supported in part by the National Science Foundation through TeraGrid resources (Catlett 2007). Computations were performed at the NCSA Abe, LONI Queen Bee, and IAS Aurora clusters. The software used in this work was in part developed by the DOE-supported ASC / Alliance Center for Astrophysical Thermonuclear Flashes at the University of Chicago.

## APPENDIX

### A. WEAK INTERACTION RATES

Here we describe the calculation of weak interaction source terms entering the energy and lepton conservation equations (eqns. [6] and [7], respectively). We only consider electron-type neutrinos and antineutrinos, as other species do not exchange energy with matter outside the neutrinosphere. Our implementation largely resembles that of Ohnishi et al. (2006), with some minor modifications.

For both species, we assume a free-streaming neutrino flux radiated isotropically from neutrinospheres located at the same radius  $R_{\nu}$ . The neutrino distributions are approximated by a Fermi-Dirac function with zero chemical potential

$$f_{\nu_i}(\epsilon, T_{\nu_i}, r, \cos \theta_k) = N_{\nu_i} F_{\text{FD}}(\epsilon, T_{\nu_i}, 0) \Theta[\cos \theta_k - \cos \theta_{\nu}(r)], \quad (\text{A1})$$

where  $\nu_i = \{\nu_e, \bar{\nu}_e\}$ ,

$$F_{\text{FD}}(\epsilon, T, \mu) = \frac{1}{\exp(\epsilon - \mu)/kT + 1} \quad (\text{A2})$$

is the Fermi-Dirac distribution with energy  $\epsilon$  and chemical potential  $\mu$ . The normalization factor

$$N_{\nu_i} = \frac{L_{\nu_i}}{(7/16)4\pi R_{\nu}^2 \sigma_{\text{SB}} T_{\nu_i}^4} \quad (\text{A3})$$

is such that the neutrino luminosity  $L_{\nu_i}$  and spectral temperature  $T_{\nu_i}$  are independent parameters. The step function  $\Theta$  contains the angular dependence of the radiation field, which propagates up to an angle

$$\theta_k < \theta_{\nu}(r) = \arccos \left[ 1 - \left( \frac{R_{\nu}}{r} \right)^2 \right]^{1/2} \quad (\text{A4})$$

from the radial direction. In equation (A3),  $\sigma_{\text{SB}}$  is the Stefan-Boltzmann constant.

To approximate the results of radiation-hydrodynamic simulations with our simplified assumptions, we set  $L_{\nu_e} = L_{\bar{\nu}_e}$  but specify different temperatures,  $T_{\nu_e} = 4$  MeV and  $T_{\bar{\nu}_e} = 6$  MeV, reflecting the fact that the photospheres are at slightly different locations, but with a spectrum such that luminosities are roughly comparable (Janka 1995, 2001). We ignore however the correction due to the spatial difference between the electron neutrino- and antineutrinospheric radius, which is of the order of 10%. This difference is absorbed by the normalization factor in equation (A3).

The evolution of  $Y_e$  above the neutrinosphere is determined by the net production rate of electron and positrons  $\Gamma_{e^-}$  and  $\Gamma_{e^+}$ , respectively (eq. [7]), due to neutrino absorption and emission. Following Bruenn (1985), these are given by

$$\Gamma_{\text{net}} = \Gamma_{e^-} - \Gamma_{e^+} \quad (\text{A5})$$

$$\Gamma_{e^-} = \frac{2\pi m_n c}{(hc)^3 \rho} \int d\cos\theta_k \int \epsilon^2 d\epsilon [\kappa_{\nu_e} f_{\nu_e} - j_{\nu_e} (1 - f_{\nu_e})] \quad (\text{A6})$$

$$\Gamma_{e^+} = \frac{2\pi m_n c}{(hc)^3 \rho} \int d\cos\theta_k \int \epsilon^2 d\epsilon [\kappa_{\bar{\nu}_e} f_{\bar{\nu}_e} - j_{\bar{\nu}_e} (1 - f_{\bar{\nu}_e})], \quad (\text{A7})$$

where  $j_{\nu_i}$  and  $\kappa_{\nu_i}$  are the emissivity and absorption coefficient, respectively, associated with electron-type neutrinos or antineutrinos (as subscripted), and the integrals are performed over all propagation angles and positive energies. Expressions for these coefficients are obtained by Bruenn (1985) assuming detailed balance, matter in nuclear statistical equilibrium, and non-relativistic nucleons, whose recoil is neglected. In addition, we ignore here the nucleon phase space blocking factors, which deviate only slightly from unity at densities  $\lesssim 10^{11}$  g cm $^{-3}$  (Bruenn 1985), yielding

$$j_{\nu_e}(\epsilon, T, \mu_e, n_p) = \frac{\tilde{G}_F^2}{\pi} (g_V^2 + 3g_A^2) n_p F_{\text{FD}}(\epsilon, T, \mu_e) [\epsilon + \Delta_m]^2 \times \left[ 1 - \frac{m_e^2 c^4}{(\epsilon + \Delta_m)^2} \right]^{1/2} \quad (\text{A8})$$

$$j_{\bar{\nu}_e}(\epsilon, T, \mu_e, n_p) = \frac{\tilde{G}_F^2}{\pi} (g_V^2 + 3g_A^2) n_n F_{\text{FD}}(\epsilon - \Delta_m, T, -\mu_e) [\epsilon - \Delta_m]^2 \times \left[ 1 - \frac{m_e^2 c^4}{(\epsilon - \Delta_m)^2} \right]^{1/2} \Theta(\epsilon - \Delta_m - m_e c^2) \quad (\text{A9})$$

$$\kappa_{\nu_e}(\epsilon, T, \mu_e, n_p) = \frac{\tilde{G}_F^2}{\pi} (g_V^2 + 3g_A^2) n_n [1 - F_{\text{FD}}(\epsilon, T, \mu_e)] [\epsilon + \Delta_m]^2 \times \left[ 1 - \frac{m_e^2 c^4}{(\epsilon + \Delta_m)^2} \right]^{1/2} \quad (\text{A10})$$

$$\kappa_{\bar{\nu}_e}(\epsilon, T, \mu_e, n_p) = \frac{\tilde{G}_F^2}{\pi} (g_V^2 + 3g_A^2) n_p [1 - F_{\text{FD}}(\epsilon - \Delta_m, T, -\mu_e)] [\epsilon - \Delta_m]^2 \times \left[ 1 - \frac{m_e^2 c^4}{(\epsilon - \Delta_m)^2} \right]^{1/2} \Theta(\epsilon - \Delta_m - m_e c^2), \quad (\text{A11})$$

where  $\mu_e$  is the chemical potential of electrons,  $n_n$  and  $n_p$  the number density of free neutrons and protons, respectively,  $\tilde{G}_F = G_F / (\hbar c)^3$  the Fermi constant,  $g_V$  and  $g_A$  the vector and axial coupling constants, respectively, and  $\Delta_m = (m_n - m_p)c^2$  the difference between the rest mass energy of neutrons and protons.

The rates of energy exchange between neutrinos and matter are similarly found as a function of  $f_{\nu_i}$ ,  $j_{\nu_i}$ , and  $\kappa_{\nu_i}$ . The heating and cooling rates per unit volume are given respectively by

$$\mathcal{L}_H = \frac{\rho}{m_n} (Q_{\nu_e}^+ + Q_{\bar{\nu}_e}^+) \quad (\text{A12})$$

$$\mathcal{L}_C = \frac{\rho}{m_n} (Q_{\nu_e}^- + Q_{\bar{\nu}_e}^-), \quad (\text{A13})$$

where  $Q_{\nu_i}^\pm$  are rates per baryon of heating (+ superscript) and cooling (- superscript) due to electron-type neutrinos ( $\nu_e$  subscript) and antineutrinos ( $\bar{\nu}_e$  subscript). These rates are given by

$$Q_{\nu_e}^+ = \frac{2\pi m_n c}{(hc)^3 \rho} \int d\cos\theta_k \int \epsilon^3 d\epsilon [j_{\nu_e} + \kappa_{\nu_e}] f_{\nu_e} \quad (\text{A14})$$

$$Q_{\bar{\nu}_e}^+ = \frac{2\pi m_n c}{(hc)^3 \rho} \int d\cos\theta_k \int \epsilon^3 d\epsilon [j_{\bar{\nu}_e} + \kappa_{\bar{\nu}_e}] f_{\bar{\nu}_e} \quad (\text{A15})$$

$$Q_{\nu_e}^- = \frac{4\pi m_n c}{(hc)^3 \rho} \int \epsilon^3 d\epsilon j_{\nu_e} \quad (\text{A16})$$

$$Q_{\bar{\nu}_e}^- = \frac{4\pi m_n c}{(hc)^3 \rho} \int \epsilon^3 d\epsilon j_{\bar{\nu}_e}. \quad (\text{A17})$$

Numerical calculation of equations (A6)-(A7) and (A14)-(A17) involves tabulating Fermi-Dirac integrals as a function of  $T$ ,  $\mu_e$ , and  $T_{\nu_i}$ , with other dependencies entering as global scaling factors. The left panel of Figure A shows the total cooling per baryon  $Q_{\text{tot}}^- = Q_{\nu_e}^- + Q_{\bar{\nu}_e}^-$  as a function of temperature, for fixed  $Y_e$  and different densities. In the degenerate regime  $kT < \pi\mu_e$ , the cooling rates are nearly independent of temperature, whereas for higher temperatures they approach the asymptotic expression  $Q_{\text{tot}}^- \simeq 145(kT/2\text{MeV})^6$  from Janka (2001), obtained by assuming zero electron chemical potential. The right panel of Figure A

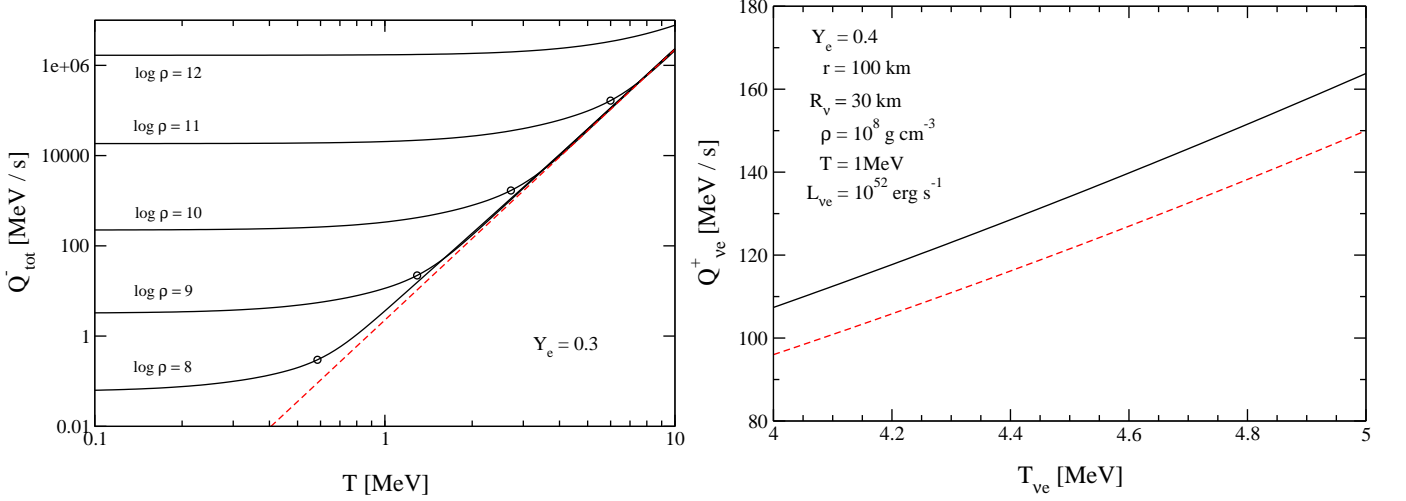


FIG. 16.— *Left*: Total cooling rate per baryon  $Q_{\text{tot}}^- = Q_{\nu e}^- + Q_{\nu \mu}^-$  (eqns. [A16]–[A17]) as a function of temperature, for fixed electron fraction  $Y_e = 0.3$ , and assuming  $X_p + X_n = 1$ . Different solid lines correspond to different densities (in g cm $^{-3}$ ), with circles marking the approximate boundary between degenerate and non-degenerate regimes, at  $\mu_e = \pi kT$ . The red dashed line shows the approximate expression  $Q_{\text{tot}}^- \simeq 145(kT/2\text{MeV})^6$  MeV s $^{-1}$ , obtained assuming non-degenerate electrons (Janka 2001). *Right*: Heating due to absorption of electron-type neutrinos (eq. [A14]) as a function of the temperature of the electron neutrinosphere  $T_{\nu e}$ , for parameters as shown in the panel. For reference, the red-line shows the approximate expression  $Q_{\nu e}^+ \simeq 160L_{\nu,52}r_7^{-2}(1-Y_e)(kT_{\nu e}/4\text{MeV})^2$  MeV s $^{-1}$  from Janka (2001).

shows heating by absorption of electron-type neutrinos as a function of  $T_{\nu e}$ , for fixed parameters as shown in the Figure. For reference, the approximate expression  $Q_{\nu e}^+ \simeq 160L_{\nu,52}r_7^{-2}(1-Y_e)(kT_{\nu e}/4\text{MeV})^2$  MeV s $^{-1}$  (Janka 2001) is also shown, agreeing with our results to within  $\sim 10\%$ .

### B. GRID OF VARIABLE SPACING IN FLASH3.2

Time-dependent modelling of post-bounce core-collapse supernova hydrodynamics demands the ability to resolve a steep density gradient in the proton-neutron star atmosphere ( $\sim 30$  km) while also allowing for the shock to expand out to at least  $\sim 1000$  km to track an explosion. For a grid in spherical coordinates, an efficient way to accomplish this is to use variable spacing in radius.

The public version of FLASH3.2 was modified to include this capability, starting from the existing *uniform grid* mode. The implementation can be decomposed into two parts. First, defining the cell sizes and coordinates appropriately when the computational domain is initialized. The second part involves modifying all the subroutines that assume a uniform grid spacing.

Grid initialization is accomplished by modifying the `Grid_init` and `gr_create_domain` subroutines. We define the grid points in between  $r_{\min}$  and  $r_{\max}$  such that consecutive cell sizes have a ratio  $\Delta r_{i+1}/\Delta r_i = \zeta > 1$ , where  $i$  is a cell index which increases with increasing radius. For a given number of grid cells  $N_r$  the ratio can be obtained by solving (e.g., Stone & Norman 1992)

$$\begin{aligned} r_{\max} - r_{\min} &= \Delta r_{\min} \sum_{i=0}^{N_r-1} \zeta^i \\ &= \Delta r_{\min} \left[ \frac{\zeta^{N_r} - 1}{\zeta - 1} \right], \end{aligned} \quad (\text{B1})$$

where  $\Delta r_{\min}$  is the minimum cell size, whose inner edge is located at  $r_{\min}$ . A logarithmic spacing can be achieved by setting  $\zeta = (r_{\max}/r_{\min})^{1/N_r}$ , which then determines the minimum cell size:  $\Delta r_{\min} = r_{\min}(\zeta - 1)$ . It then follows that for  $0 \leq q \leq N_r$ ,

$$\frac{\Delta r_q}{r_q} = \frac{\zeta^q}{(r_q/r_{\min})} \frac{\Delta r_{\min}}{r_{\min}} = \frac{\Delta r_{\min}}{r_{\min}}, \quad (\text{B2})$$

with  $r_0 = r_{\min}$  and  $r_{N_r} = r_{\max}$ .

There are only three subroutines that make the assumption of a uniform grid when using spherical coordinates. They are `hy_ppm_sweep`, `Driver_computeDt`, and `Driver_verifyInitDt`. In all three cases, a scalar cell spacing was replaced with a vector in the appropriate locations. The subroutines that compute cell areas and volumes make direct use of coordinate information, so no additional modification is required for spherical coordinates.

As a test of the grid implementation, we have run the self-similar explosion problem of Sedov (1982). An energy  $E_0$  is initially placed inside some spherical volume with a radius smaller than some characteristic radius  $R_0$ . The medium has uniform density  $\rho_0$ , and has an ideal gas equation of state with adiabatic index  $\gamma$ . Outside of the injection volume, the pressure is uniform and equal to  $10^{-5}E_0R_0^{-3}$ . Our benchmark simulation has 500 cells uniformly spaced in radius from  $r = 0$  to  $r = R_0$ . The energy is placed in the first grid cell, with radius  $r_{\text{inj}} = 2 \times 10^{-3}R_0$ , and we set  $\gamma = 1.4$ .

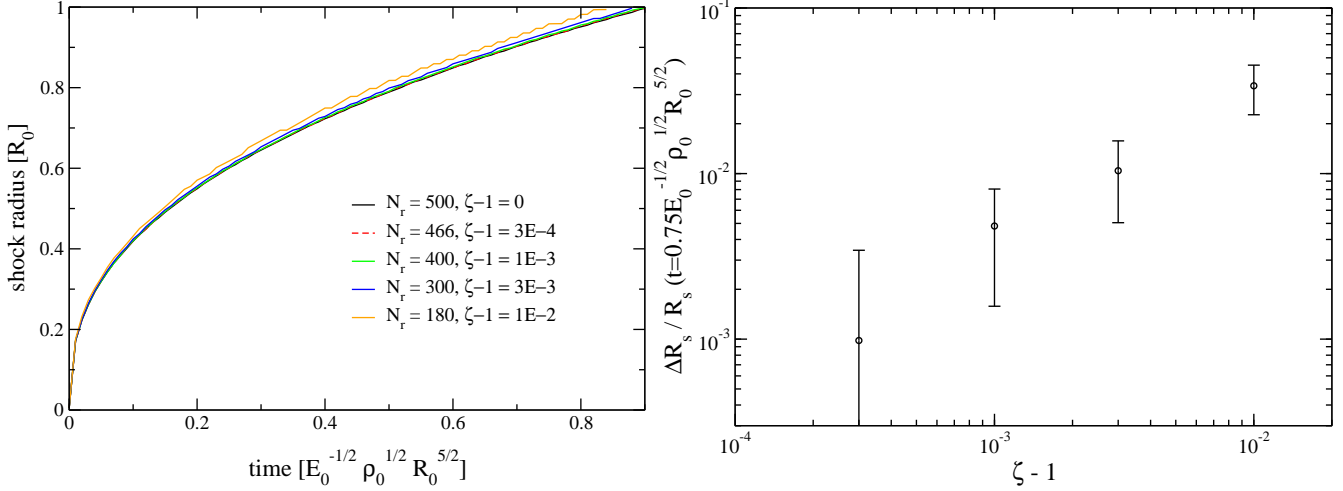


FIG. 17.— Strong explosion problem of Sedov (1982), used here as a test of the non-uniform grid implementation in FLASH3.2. The left panel shows the shock trajectory as a function of time, with colors labeling resolutions as shown in the caption. The minimum cell size next to the origin is kept equal to the uniform grid case ( $\zeta = 1$ ). The right panel shows the fractional deviation from the shock position at time  $0.75E_0^{-1/2} \rho_0^{1/2} R_0^{5/2}$  in the  $N_r = 500$  run, with error bars indicating the cell sizes in each simulation at their respective shock positions, normalized to the shock position in the  $N_r = 500$  run.

We then run a sequence of simulations that preserve the minimum cell spacing next to the origin,  $\Delta r_{\min} = r_{\text{inj}}$ , but vary the number of cells, resulting in a ratioed (not logarithmic) grid that satisfies equation (B1). The number of cells are  $N_r = \{466, 400, 300, 180\}$  which results in  $(\zeta - 1) \simeq \{3 \times 10^{-4}, 10^{-3}, 3 \times 10^{-3}, 10^{-2}\}$ , respectively. The left panel of Figure B shows the shock radius (obtained by linear interpolating the location of the surface with pressure  $10^{-3}E_0R_0^{-3}$ ) as a function of time for the sequence of runs. As the number of cells is decreased relative to the benchmark model, the cells in the upper part of the domain become increasingly coarser, and the shock trajectory gradually diverges from the uniform grid case. The right panel of Figure B shows the fractional deviation from the uniform grid result at a time  $0.75E_0^{-1/2} \rho_0^{1/2} R_0^{5/2}$ , with the error bars indicating the fractional size of the cell at the given shock position, normalized to the shock position in the benchmark model. As the spacing ratio decreases, deviations tend to zero close to linearly in  $(\zeta - 1)$ .

### C. NUMERICAL CALCULATION OF THE RATE OF CHANGE OF ENERGY

Here we describe the calculation of the different terms that comprise the rate of change of the total energy with time (eq. [19]) for Figures 5 and 7.

In the Piecewise Parabolic Method (Colella & Woodward 1984) used in FLASH, the shock is typically broadened along 2-3 cells. To compute an accurate shock position, we begin by finding the minimum in the radial derivative of the pressure. We establish a reference position by taking a weighted average of the radial coordinate, with weight equal to  $|\partial p / \partial r|$  around the minimum. This reference position, which varies smoothly with time, is a good tracer of the center of the shock. Because we want quantities below the shock, we define our actual shock position to be a fixed distance (of the order of two cell widths) behind the center of the shock, so that the fluid quantities are in the post-shock regime while remaining as close to the shock center as possible.

Next, the energy flux entering through the shock  $\dot{E}_{\text{up}}$  (eq. [21]) is computed by interpolating variables (linearly for velocity and internal energy; logarithmically for pressure and density) to the shock position. The energy flux leaving the domain  $\dot{E}_{\text{dn}}$  (eq. [22]) is computed at a radius  $R_{\text{in}}$  corresponding to the inner edge of some cell inside the domain. After some experimentation, we found that the innermost location that is not significantly affected by boundary effects is the third active cell from the inner boundary at  $R_{\text{in}}$ . To compute the energy flux at  $R_{\text{in}}$ , we average the fluid variables from the cells that this radius separates as an approximation to face-centered values. The integrated neutrino source terms  $\dot{E}_{\text{N}}$  (eq. [20]) are computed by simple integration of the cells fully contained between  $R_{\text{in}}$  and the shock, and then a small differential term is added by linear interpolation,  $4\pi R_{\text{out}}^2 \mathcal{L}_{\text{net}} \Delta R$ , where  $R_{\text{out}}$  is the outer radius of the cell that is closest to and fully contained within the shock surface, and  $\Delta R = R_{\text{S}} - R_{\text{out}}$ . The shock motion term  $\dot{E}_{\text{S}}$  is found by first computing the shock velocity through time-centered finite differences, and then evaluating fluid quantities at the same position as for  $\dot{E}_{\text{up}}$ .

For calibration, we also compute the total energy contained between  $R_{\text{in}}$  and the shock. The total rate of change, computed through time-centered finite differences, and the sum of the separate terms that make it up (eq. [19]) are shown in Figure 18. Quantities are sampled every 2 ms to eliminate high frequency noise. Agreement is very good if a zero point, equal to the sum of all the terms that make up  $\dot{E}_{\text{tot}}$  at  $t = 0$ , is subtracted.

Also shown in Figure 18 is the net energy generation from accretion,  $\dot{E}_{\text{N}} - \dot{E}_{\text{up}} + \dot{E}_{\text{dn}}$ , together with what is obtained if the shock motion term  $\dot{E}_{\text{S}}$  is subtracted from the total rate of change of the energy  $\dot{E}_{\text{tot}}$ , computed from finite differencing the total energy. Agreement is again very good if the same zero point is subtracted. This smoother version of the accretion energy generation,

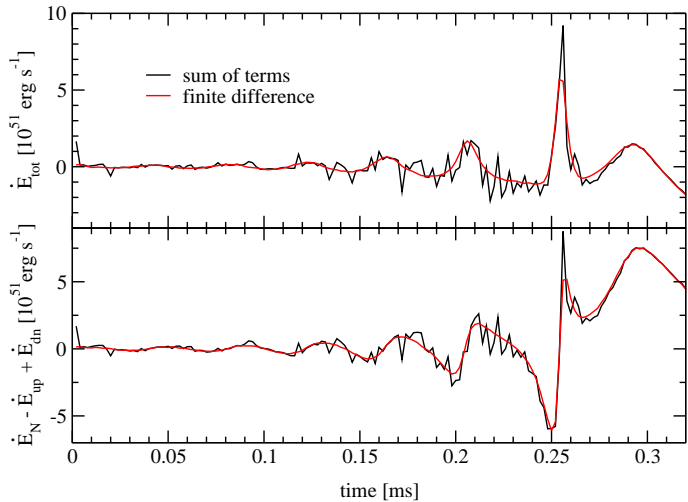


FIG. 18.— *Top*: evolution of the total energy in the model shown in Figure 5. The black curve corresponds to the sum of the terms on the right hand side of equation (19), calculated as described in the text. The red curve is a time-centered finite difference derivative of the instantaneous total energy. *Bottom*: evolution of the net energy generation from accretion. The black curve is the sum of the terms that comprise it, while the red curve is obtained by subtracting the energy generation from shock motion  $\dot{E}_s$  from the red curve in the top panel.

together with  $\dot{E}_{\text{tot}}$  from finite differencing, is what is shown in Figures 5 and 7.

## REFERENCES

- Bethe, H. A. 1990, *Reviews of Modern Physics*, 62, 801  
 —. 1996, *ApJ*, 469, 737  
 Bethe, H. A., & Wilson, J. R. 1985, *ApJ*, 295, 14  
 Blondin, J. M., Mezzacappa, A., & DeMarino, C. 2003, *ApJ*, 584, 971  
 Bruenn, S. W. 1985, *ApJS*, 58, 771  
 Buras, R., Janka, H.-T., Rampp, M., & Kifonidis, K. 2006a, *A&A*, 457, 281  
 Buras, R., Rampp, M., Janka, H.-T., & Kifonidis, K. 2006b, *A&A*, 447, 1049  
 Burrows, A., Dessart, L., & Livne, E. 2007a, in *American Institute of Physics Conference Series*, Vol. 937, *Supernova 1987A: 20 Years After: Supernovae and Gamma-Ray Bursters*, ed. S. Immler, K. Weiler, & R. McCray, 370–380  
 Burrows, A., & Goshy, J. 1993, *ApJ*, 416, L75  
 Burrows, A., Hayes, J., & Fryxell, B. A. 1995, *ApJ*, 450, 830  
 Burrows, A., Livne, E., Dessart, L., Ott, C. D., & Murphy, J. 2007b, *ApJ*, 655, 416  
 Catlett, C. e. a. 2007, in *HPC and Grids in Action*, ed. L. Grandinetti (Amsterdam: IOS Press)  
 Colella, P., & Woodward, P. R. 1984, *Journal of Computational Physics*, 54, 174  
 Cox, J. P. 1974, *Rep. Prog. Phys.*, 37, 563  
 Dubey, A., Antypas, K., Ganapathy, M. K., Reid, L. B., Riley, K., Sheeler, D., Siegel, A., & Weide, K. 2009, *J. Par. Comp.*, 35, 512  
 Eddington, A. S. 1926, *The internal constitution of the stars*, 1st edn. (Cambridge: Cambridge Univ. Press)  
 Fernández, R., & Thompson, C. 2009a, *ApJ*, 703, 1464  
 —. 2009b, *ApJ*, 697, 1827  
 Foglizzo, T. 2009, *ApJ*, 694, 820  
 Foglizzo, T., Galletti, P., Scheck, L., & Janka, H.-T. 2007, *ApJ*, 654, 1006  
 Foglizzo, T., Scheck, L., & Janka, H.-T. 2006, *ApJ*, 652, 1436  
 Hanke, F., Marek, A., Müller, B., & Janka, H.-T. 2011, *ApJ*, submitted, arXiv:1108.4355  
 Iwakami, W., Kotake, K., Ohnishi, N., Yamada, S., & Sawada, K. 2008, *ApJ*, 678, 1207  
 Janka, H.-T. 1995, *Astroparticle Physics*, 3, 377  
 —. 2001, *A&A*, 368, 527  
 Janka, H.-T., & Keil, W. 1998, in *Supernovae and cosmology*, ed. L. Labhardt, B. Binggeli, & R. Buser, 7  
 Janka, H.-T., & Müller, E. 1996, *A&A*, 306, 167  
 Kitaura, F. S., Janka, H.-T., & Hillebrandt, W. 2006, *A&A*, 450, 345  
 Landau, L. D., & Lifshitz, E. M. 1987, *Fluid Mechanics*, 2nd edn. (Oxford: Butterworth-Heinemann)  
 Liebendörfer, M., Mezzacappa, A., Thielemann, F.-K., Messer, O. E., Hix, W. R., & Bruenn, S. W. 2001, *PRD*, 63, 103004  
 Marek, A., & Janka, H.-T. 2009, *ApJ*, 694, 664  
 Murphy, J. W., & Burrows, A. 2008, *ApJ*, 688, 1159  
 Murphy, J. W., & Meakin, C. 2011, *ApJ*, in press, arXiv:1106.5496  
 Nordhaus, J., Burrows, A., Almgren, A., & Bell, J. 2010, *ApJ*, 720, 694  
 O’Connor, E., & Ott, C. D. 2010, *Clas. Quant. Grav.*, 27, 4103  
 Ohnishi, N., Kotake, K., & Yamada, S. 2006, *ApJ*, 641, 1018  
 Pejcha, O., & Thompson, T. A. 2011, *ApJ*, submitted, arXiv:1103.4864  
 Rampp, M., & Janka, H.-T. 2002, *A&A*, 396, 361  
 Sato, J., Foglizzo, T., & Fromang, S. 2009, *ApJ*, 694, 833  
 Scheck, L., Janka, H.-T., Foglizzo, T., & Kifonidis, K. 2008, *A&A*, 477, 931  
 Scheck, L., Kifonidis, K., Janka, H.-T., & Müller, E. 2006, *A&A*, 457, 963  
 Sedov, L. I. 1982, *Similarity and Dimensional Methods in Mechanics*, ninth edn. (Moscow: Mir Publishers)  
 Shen, H., Toki, H., Oyamatsu, K., & Sumiyoshi, K. 1998, *Nuc. Phys. A*, 637, 435  
 Stone, J. M., & Norman, M. L. 1992, *ApJS*, 80, 753  
 Sumiyoshi, K., Yamada, S., Suzuki, H., Shen, H., Chiba, S., & Toki, H. 2005, *ApJ*, 629, 922  
 Suwa, Y., Kotake, K., Takiwaki, T., Whitehouse, S. C., Liebendörfer, M., & Sato, K. 2010, *PASJ*, 62, L49  
 Thompson, C. 2000, *ApJ*, 534, 915  
 Thompson, T. A., Burrows, A., & Pinto, P. A. 2003, *ApJ*, 592, 434  
 Thompson, T. A., Quataert, E., & Burrows, A. 2005, *ApJ*, 620, 861  
 Unno, W., Osaki, Y., Ando, A., & Shibahashi, H. 1989, *Nonradial Oscillations of Stars*, 1st edn. (Tokyo: Univ. Tokyo Press)  
 Wilson, J. R., Mayle, R., Woosley, S. E., & Weaver, T. 1986, *Annals of the New York Academy of Sciences*, 470, 267  
 Wongwathanarat, A., Janka, H.-T., & Müller, E. 2010, *ApJ*, 725, L106  
 Yamasaki, T., & Yamada, S. 2005, *ApJ*, 623, 1000  
 —. 2006, *ApJ*, 650, 291  
 —. 2007, *ApJ*, 656, 1019